

Panchromatic Estimation of Star Formation Rates in BzK Galaxies at $1 < z < 3$

Peter Kurczynski¹, Eric Gawiser¹, Minh Huynh², Rob J. Ivison³, Ezequiel Treister⁴, Ian Smail⁵, Guillermo A. Blanc⁶, Carolin N. Cardamone⁷, Thomas R. Greve⁸, Eva Schinnerer⁸,
Meg Urry¹¹, Paul van der Werf^{9,10}, Fabian Walter⁸

Received _____; accepted _____

¹Department of Physics and Astronomy, Rutgers University, Piscataway, NJ 08854, USA

²Infrared Processing and Analysis Center, MS 220-6, California Institute of Technology, Pasadena, CA 91125, USA

³UK Astronomy Technology Centre, Royal Observatory, Blackford Hill, Edinburgh EH9 3HJ, UK

⁴Institute for Astronomy, 2680 Woodlawn Drive, University of Hawaii, Honolulu, HI 96822, USA.

⁵Institute for Computational Cosmology, Department of Physics, Durham University, South Road, Durham DH1 3LE, UK

⁶Department of Astronomy, The University of Texas at Austin, Austin, USA

⁷Physics Department, Massachusetts Institute of Technology, Cambridge, MA 02139, USA

⁸MPI for Astronomy, Königstuhl 17, 69117 Heidelberg, Germany

⁹Leiden Observatory, Leiden University, PO Box 9513, NL - 2300 RA Leiden, The Netherlands

¹⁰SUPA, Institute for Astronomy, University of Edinburgh, Royal Observatory, Blackford Hill, Edinburgh EH9 3HJ, UK

¹¹Department of Physics, Yale University, P.O. Box 208121, New Haven, CT 06520-8121, USA

ABSTRACT

We determine Star Formation Rates (SFRs) in a sample of color selected, star forming (sBzK) galaxies ($K_{AB} < 21.8$) in the Extended Chandra Deep Field - South (ECDF-S). To avoid AGN, we eliminate 12% of the original sample that have X-ray detections in Chandra catalogs. X-ray stacking, including in the 4 Ms CDF-S, shows that the remaining 597 sBzK galaxies are not dominated by obscured AGN. Photometric redshift binned, average flux densities are measured with stacking analyses in Chandra, Spitzer-MIPS, sub-millimeter, and radio data. We include averages of aperture fluxes in MUSYC UBVRiz/JHK images to determine UV-through-radio Spectral Energy Distributions (SEDs). We determine total IR luminosities, compare SFR calibrations from X-ray, UV, 24 μm , FIR and radio wavebands, and we find preferred calibrations for each waveband. We find consistency with our best estimator, SFR_{IR+UV} , to within a factor of two for dust corrected UV and the preferred radio SFR calibration. Our results show that 24 μm -only and X-ray SFR estimates should be used with caution. Average IR luminosities are consistent with Luminous Infrared Galaxies. We find SFR_{IR+UV} for stacked sBzKs at median redshifts 1.1, 1.4, 1.8, 2.2 to be 12 ± 3 , 58 ± 7 , 100 ± 14 , $130 \pm 28 \text{ M}_{\odot} \text{ yr}^{-1}$ respectively. Extrapolated to deeper samples, these galaxies appear to contribute $\sim 20\%$ to the cosmic star formation rate density in the range $1.5 < z \leq 2$.

Subject headings: submillimeter: general, infrared: general, radio continuum: general, galaxies: statistics, galaxies: high redshift

1. Introduction

The history of star formation traces the origins of visible matter in the universe. Understanding star formation across cosmic time will yield insights into diverse areas of astronomy from the formation and evolution of galaxies to the initial conditions of stellar evolution. The redshift range $1 < z < 3$ is a key epoch in this history, when most of the stars in the universe were born; however, the systematic study of star formation in this range has not yet been accomplished. High redshift galaxies are identified with color selection methods; however, these methods introduce selection biases. Estimating their star formation rates (SFRs) is complicated by contamination from Active Galactic Nuclei (AGN), and other sources of systematic uncertainty that include the initial mass function (IMF; used to extrapolate calibrations based on observations of massive stars to the entire stellar population), photometric redshifts (used to convert flux to luminosity), spectral energy distributions (used to estimate luminosities and correct for dust), and SFR calibrations (used to estimate SFR from the observed luminosity in a particular waveband).

1.1. SFR Calibrations

SFRs in the local universe are estimated from a wide variety of luminosity calibrations from X-ray through radio wavebands, see e.g. Kennicutt (1998); Calzetti (2008). Locally, dust corrected SFR estimates are believed to be precise to within a factor of two, notwithstanding potential systematic uncertainty caused by the IMF (Kennicutt et al. 2009). However, systematics impact even the most accurate calibrations of high redshift star formation (Reddy et al. 2010; Yoshikawa et al. 2010; Garn et al. 2010).

The most reliable SFR calibration comes from dust extinction corrected, Hydrogen emission line spectroscopy, which measures ionizing UV radiation from young stars.

However, rest frame optical spectroscopy is particularly difficult to obtain for high redshift galaxies. Broadband UV continuum radiation directly probes the light of young stars; however, dust attenuation peaks in the UV and causes both extinction and spectral reddening. UV slope based corrections for this attenuation (Meurer et al. 1999) are not universally applicable, particularly for low luminosity galaxies in the nearby universe (Buat et al. 2010), and the situation at high redshift is less clear.

IR luminosity, hereafter defined as $L_{IR} \equiv L(8 - 1000 \mu m)$, estimates dust obscured star formation, but may miss young stars that have escaped their birth clouds. In low SFR galaxies, it may be confused by IR cirrus – emission from old, passive stars that tend to be more uniformly distributed within a galaxy compared to clumpy star forming regions (Kennicutt 1998). Because IR and uncorrected UV luminosities sum reprocessed and un-reprocessed photons from star forming regions to get the total luminosity emitted by young stars, the sum of IR and uncorrected UV SFRs are used to estimate total SFR in high redshift galaxies. This trend follows that used in the local universe where linear combinations of unobscured and obscured SFR estimates are being employed (Kennicutt et al. 2009).

X-ray (2-10 keV) luminosity in star forming galaxies arises from high mass X-ray binaries (HMXBs), consisting of short lived, massive ($M > 8M_{\odot}$) stars with a neutron star companion, low mass X-ray binaries (LMXBs), consisting of long lived, low mass ($M < 1M_{\odot}$) stars with neutron star companions¹ and to a lesser extent, supernova remnants (SNRs) (Persic & Rephaeli 2002). These multiple sources of X-ray emission, as well as X-ray obscuration by gas and dust, complicate SFR X-ray calibration.

¹intermediate mass stars $1 < M < 8M_{\odot}$, are not believed to give rise to long lived X-ray luminosity

Radio wave (1.4 GHz) luminosity in star forming galaxies, which is unobscured by dust, arises from synchrotron emission from supernova remnants (SNRs; $\sim 90\%$) and thermal free-free emission ($\sim 10\%$), and therefore is linked to young, massive stars (Condon 1992). Some radio wave SFR calibrations (Bell 2003; Yun et al. 2001) and X-ray SFR calibrations (Ranalli et al. 2003) explicitly rely upon empirical correlations between luminosities in their respective wavebands and IR luminosity; therefore, they are indirect measures of IR luminosity.

Because of the different assumptions and confounding factors in SFR calibrations, there is a great need for systematic comparison of these methods in high redshift galaxies. In this investigation, we use multiwavelength data to estimate SFRs within a population of high redshift galaxies using a variety of the most commonly used calibrations. By comparing these estimates to the total SFR, estimated from IR and uncorrected UV luminosity, we seek to test their robustness at high redshift.

1.2. sBzK Galaxies

To study star formation in the redshift range of peak star formation density in the universe, we selected BzK galaxies. The BzK color selection criterion (Daddi et al. 2004), has emerged as a successful color based method for identifying galaxies in the range $1.4 \lesssim z \lesssim 2.5$ in a maximally inclusive manner. Daddi et al. (2004) defined the quantity BzK as

$$BzK \equiv (z - K)_{AB} - (B - z)_{AB} \quad (1)$$

They found that actively star forming galaxies, sBzKs, can be selected by requiring $BzK > -0.2$, the upper left region in Figure 1. The reddening vector in the BzK plane is parallel to the BzK line, making this selection unbiased with respect to dust content. The reddest galaxies in both $z-K$ and $B-z$ tend to be old, passively evolving stellar systems at $z > 1.4$

and are known as pBzKs, and are located in the upper right region of Figure 1.

sBzKs have been studied in the Great Observatories Origins Deep Survey (GOODS) (Reddy et al. 2005; Daddi et al. 2007b)(and references therein), Deep3a-F and “Daddi” fields (Dannerbauer et al. 2006; Kong et al. 2006), United Kingdom Infrared Deep Sky Survey (UKIDSS) (Lane et al. 2007; Dunne et al. 2009), Subaru Deep Field (Hayashi et al. 2007), Subaru/XMM-Newton Deep Field (SXDF) (Takagi et al. 2008), COSMOS (McCracken et al. 2010) and ECDF-S (Blanc et al. 2008; Greve et al. 2010) and the Multiwavelength Survey by Yale-Chile (MUSYC) 1030 and 1255 fields (Blanc et al. 2008).

sBzK galaxies are found in $K_{AB} < 22$ surveys to be typically massive, ($M \sim 10^{11} M_{\odot}$), luminous ($L \sim 10^{11-12} L_{\odot}$) galaxies that are not dominated by AGN. They are highly clustered and moderately abundant, with a surface density of $\sim 1 \text{ arc min}^{-2}$, and a comoving volume density of $\gtrsim 10^{-4} \text{ Mpc}^{-3}$. They are found with a steeply increasing number density with magnitude in the deepest surveys reported.

SFR estimates for this population range from several tens to $600 M_{\odot} \text{ yr}^{-1}$ (see e.g. Daddi et al. 2004, 2005; Reddy et al. 2005), with average SFRs estimated from various methods typically in the range $\sim 100\text{-}200 M_{\odot} \text{ yr}^{-1}$ (Daddi et al. 2005, 2007b; Reddy et al. 2006; Dunne et al. 2009; Pannella et al. 2009; Greve et al. 2010; Yoshikawa et al. 2010). Some individual BzKs have been detected as submillimeter galaxies and estimated at $1000 M_{\odot} \text{ yr}^{-1}$ (Takagi et al. 2008), comparable to the most actively star forming galaxies known.

sBzKs may be important contributors to the cosmic star formation rate density. In order to better understand star formation in these galaxies and their contribution to the cosmic star formation history, we investigate their star formation rates binned according to photometric redshift, and stacked in radio through X-ray wavebands. In particular, we use extensive far IR-submillimeter data, for which we have an improved stacking algorithm (Kurczynski & Gawiser 2010). We discuss observations and data in Section 2. Section 3

presents the stacking methodology. We discuss our estimates of IR luminosity and SFRs in Section 4. In Section 5, we compare these estimates of star formation, and we estimate the contribution of these galaxies to the cosmic star formation rate density in the range $0.9 < z \leq 3.2$. Throughout this paper, magnitudes are measured in the AB system unless stated otherwise. We assume a Salpeter (1955) IMF from 0.1 - 100 M_{\odot} . Other commonly used IMFs, e.g. that of Kroupa (2001), change the slope of the low mass end of the IMF, and would multiply the SFRs presented here by factors of 0.5 - 0.77 (Hopkins 2007). We adopt a cosmology with $\Omega_{\Lambda} = 0.7$, $\Omega_0 = 0.3$, $h_{100} = 0.7$.

2. Sample Selection

The Extended Chandra Deep Field - South (ECDF-S) is an extensively studied field in the constellation Fornax (RA $03^h32^m29.0^s$, Dec $-27^{\circ}48'47''$) that was initially observed with the *Chandra X-ray Observatory*. The Multiwavelength Survey by Yale-Chile (MUSYC) provides data for the ECDF-S in UBVRIz'JHK bands (Gawiser et al. 2006). The MUSYC K band source catalog (Taylor et al. 2009) contains more than 8,000 sources with $K_{AB} < 22$ in the ECDF-S with photometric or spectroscopic redshifts. The MUSYC optical catalog (Cardamone et al. 2010) contains $\sim 40,000$ galaxies to $R_{AB} < 25.3$ and includes photometry from 32 bands including 18 medium band optical filters. Photometric redshifts for the optical catalog were obtained with the EAZY software (Brammer et al. 2008) and are estimated to have an average error of $\delta z / (1 + z) = 0.009$ based upon comparison with available spectroscopic redshifts from the literature (Cardamone et al. 2010). Photometric or spectroscopic redshifts are assigned to sBzK galaxies by matching positions in the K band source catalog with the MUSYC optical catalog and using redshifts from the optical catalog where redshifts in both catalogs are available.

Our catalog of 725 sBzK galaxies with $K_{Vega} < 20$ ($K_{AB} < 21.8$) is taken from Blanc

et al. (2008), and includes 640 (85) galaxies with photometric (spectroscopic) redshifts. Of this sample, 38 galaxies have $z < 0.9$ and are rejected as low redshift contaminants. Individually detected X-ray sources are removed from the sample by cross matching the sBzK positions with the combined Chandra ECDF-S and CDF-S X-ray catalogs; 90 galaxies have an X-ray source within $2''$ radius of the K band position, and thus are rejected as AGN. Possible residual AGN contamination, arising from heavily obscured sources at the highest redshifts, is discussed in Section 5.

Comparison of BzK values from our data set to the original criterion defined by Daddi et al. (2004) requires a color correction. The Bessel B band filter used on the Very Large Telescope (VLT) in the original sample of Daddi et al. (2004) is bluer than the Johnson B band filter on WFI, Suprime-Cam and other instruments, and therefore a color correction must be made to match the BzK criterion in data from these instruments. Not accounting for this correction can lead to an offset of 0.5 mag toward lower values in $(B - z)$ color and 0.04 mag in higher $(z - K)$ color, producing a significant excess of “sBzK” galaxies that are in fact low redshift contaminants (Blanc et al. 2008). The BzK color-color diagram, shown in Figure 1, has colors corrected to be consistent with the Daddi et al. (2004) selection region.

The final sample of 597 sBzKs with redshift $0.9 < z \leq 3.2$ are binned according to redshift into approximately 1 Gyr intervals in cosmic time: $0.9 < z \leq 1.2$, $1.2 < z \leq 1.5$, $1.5 < z \leq 2.0$ and $2.0 < z \leq 3.2$. The redshift binned sets are illustrated in a BzK diagram in Figure 1, and further details are included in Table 1. These sets are used in stacking analyses to determine their aggregate fluxes as discussed below.

There are 43 sBzK galaxies in the range $z \geq 0.9$ with both photometric and spectroscopic redshifts available. Histograms of photometric and spectroscopic redshift are illustrated in Figure 2. These histograms indicate that the majority of sBzKs fall in the

traditional redshift range associated with BzK galaxies, $1.4 < z < 2.5$. There are significant numbers of sBzKs at lower (8%) and higher (26%) redshifts, although BzK selection is less efficient in these ranges. Spectroscopic redshifts are taken from the literature, for which there are substantial selection biases; therefore we do not expect the distribution of spectroscopic redshifts to match precisely the distribution of photometric redshifts. Thus, the trend of spectroscopic redshifts being distributed at somewhat higher redshifts than the photometric redshifts, apparent from Figure 2, is not necessarily an indication of systematic photometric redshift error.

Photometric redshift errors, defined as $(z_{phot} - z_{spec})/(1 + z_{spec})$, are well described by a Gaussian with mean = -0.02 and $\sigma=0.08$ among the 43 sBzKs for which both redshifts are available, see Figure 3. Photometric redshift error for these galaxies is plotted vs. spectroscopic redshift in Figure 3, and compared to the distribution of photometric redshift errors for the larger sample of 1285 *K* selected galaxies with both redshifts available. 1σ and 2σ regions are indicated by shading in the figure. Three sBzK galaxies have photometric redshifts that are more than 2σ outliers.

3. Multiwavelength Observations and Stacking Analyses

We measure the multiwavelength spectral energy distributions of our sample of 597 redshift binned sBzK galaxies, and we use these data to trace star formation as a function of redshift. Most of these galaxies are not individually detected in X-ray, far IR-submillimeter and radio wavebands; therefore, stacking analysis, using the *K* band positional priors, is essential.

X-ray. X-ray exposure in the ECDF-S consists of 4 Ms in the central $\approx 16' \times 16'$ Chandra Deep Field - South, reaching approximate sensitivities of 1×10^{-17} and 7×10^{-17} erg

$\text{cm}^{-2} \text{ s}^{-1}$ in the 0.5-2.0 and 2.0-8 keV bands, respectively, and giving this field the deepest X-ray coverage to date.² These data are augmented with 4 flanking 250 ks exposures that complete the $\approx 30' \times 30'$ ECDF-S field, and reach sensitivity limits of 1.7×10^{-16} and $3.9 \times 10^{-16} \text{ erg cm}^{-2} \text{ s}^{-1}$ in the 0.5-2.0 and 2.0-8.0 keV bands, respectively (Lehmer et al. 2005; Virani et al. 2006).

Excluding individually detected galaxies, we stack 27, 82, 113, 75 source positions in redshift bins from $0.9 < z \leq 1.2$, $1.2 < z \leq 1.5$, $1.5 < z \leq 2.0$ and $2.0 < z \leq 3.2$ respectively. Background subtracted counts are converted to flux density assuming a power law photon spectrum index, $\Gamma = 1.2$ and cut off energy $E_c = 20 \text{ keV}$. This spectrum slope is consistent with the observed spectrum of high-mass X-ray binaries (Lutovinov et al. 2005), which is expected to dominate the X-ray emission from star-forming galaxies, e.g. (Persic & Rephaeli 2002).

The X-ray fluxes are presented in Table 2; they are somewhat lower than previously reported values. In stacking 59 (175) mid IR bright (mid IR normal) sBzKs in GOODS-S, Daddi et al. (2007a) reported soft band fluxes $1.1 (1.0) \times 10^{-17} \text{ erg s}^{-1} \text{ cm}^{-2}$; these values are larger by factors of 1-9 than our reported values. Daddi et al. (2007a) reported hard band fluxes of $5.6 (1.6) \times 10^{-17} \text{ erg s}^{-1} \text{ cm}^{-2}$, which are closer to our reported values. As discussed in Section 5.4, we expect that our soft band flux estimates are affected by significant intrinsic absorption from column density of $N_H \sim 10^{22} \text{ cm}^{-2}$; consequently we view with caution the SFRs estimated from these soft band fluxes.

UV-Optical-NIR. MUSYC 5σ imaging depths are $U = 26.5$, $B=26.9$, $V=26.6$, $R=26.3$, $I=24.8$, $z'=24.0$, $J =23.1$, $H=22.4$, $K=22.4$. Details on the imaging can be found

²Sensitivity estimates are based upon the 2Ms data; a catalog of the 4Ms data set has not yet been released.

in Gawiser et al. (2006) and Taylor et al. (2009). Galaxies are individually measured in MUSYC UBVRIz/JHK bandpasses via aperture photometry, and their fluxes in each redshift bin are combined in an inverse variance weighted average (justified due to errors being background dominated) to yield average fluxes for each bandpass. These average fluxes for redshift binned sBzKs in each UV-radio waveband are indicated in Table 3.

MIPS 24, 70 μm . Infrared data were obtained from the *Spitzer Space Telescope* Multi Band Imaging Photometer (MIPS) 24 μm and 70 μm images that reach 5σ depths of 50 μJy and 3 mJy, respectively (FIDEL, Dickinson et al. in prep). *K* band sBzK positions are compared to the 24 μm (70 μm) catalog, with a 2'' (4'') separation as the criterion for individual detection in each MIPS band, respectively. Individual detections are removed from the list for stacking. In 24 μm data, in redshift bins from $0.9 < z \leq 1.2$, $1.2 < z \leq 1.5$, $1.5 < z \leq 2.0$ and $2.0 < z \leq 3.2$, there are 8, 65, 98, 68 individual detections and 41, 89, 122 and 81 stacked positions, respectively. Similarly, in 70 μm data, in these same redshift bins, there are 2, 6, 11, 3 individual detections and 47, 147, 209, 146 stacked positions. Stacking is performed on a residual image, after removing the matched sources from the list, as summarized in Huynh et al. (2007). The stacking algorithm computes an inverse variance weighted average of the flux at each stack position. We use an ordinary average of the individual detections and the stacking detection to yield a single combined estimate for the flux of each set of galaxies. We show in Section 7 that, although the difference between these two approaches is small, the ordinary average is preferred because the weighted average can introduce a bias to the combined flux estimate.

BLAST 250, 350, 500 μm . Submillimeter data at 250, 350, 500 μm were obtained from the public archive of the Balloon-borne Large Area Space Telescope (BLAST) survey of the ECDF-S, which reaches 1σ depths of 36, 31, 20 mJy at 250, 350 and 500 μm , respectively, in an 8.7 deg² wide field and 1σ depths of 11, 9, 6 mJy at 250, 350, 500 μm in

a 0.8 deg^2 deep field (Devlin et al. 2009).

The redshift binned sBzKs are stacked in the public BLAST ‘smooth’ data (variance-weighted correlation between the signal maps and the effective point-spread functions). Each pixel in these data products represented the maximum likelihood flux density (Jy) of an isolated point source centered over the pixel (Truch et al. 2008).

We use an improved submillimeter stacking and deblending algorithm for stacking in 250, 350, 500 and $870 \mu\text{m}$ data that deals effectively with the problem of confusion (Kurczynski & Gawiser 2010). Confusion severely limits the effectiveness of stacking in deep surveys with limited angular resolution (Condon 1974; Hogg 2001), particularly at far IR-submillimeter wavelengths, and causes a bias in stacking results. Deblending corrects measured fluxes for confusion from these adjacent sources. This stacking and deblending algorithm greatly reduces bias in the flux estimate with nearly minimum variance. For more details, see Kurczynski & Gawiser (2010). All galaxies in the MUSYC catalog with $K_{AB} < 22$ are used in the deblending calculations.

We find stacking detections (defined as $\text{SNR} \geq 3$) in the $250 \mu\text{m}$ data for the redshift bin $1.5 < z \leq 2.0$ ($\text{SNR} = 12$), and in the $350 \mu\text{m}$ data for the redshift bins $1.2 < z \leq 1.5$ ($\text{SNR} = 3$) and $1.5 < z \leq 2.0$ ($\text{SNR}=10$), and in the $500 \mu\text{m}$ data, for the redshift bin $1.5 < z \leq 2.0$ ($\text{SNR}=10$). See Table 3 for the stacked flux densities and errors in each waveband. In the SED fits discussed below, the measured fluxes of formal non-detections and their appropriate error bars are included in the fits. Combining all of the BzK galaxies, without regard to redshift binning, yields stacking detections in 250, 350, $500 \mu\text{m}$ data of $3.9 \pm 0.4 \text{ mJy}$, $2.5 \pm 0.3 \text{ mJy}$, $1.8 \pm 0.2 \text{ mJy}$ respectively. Fluxes reported from stacking BzK galaxies in the same field, selected from a different K band catalog, with a different stacking algorithm are larger by about a factor of two than those values presented here (Marsden et al. 2009). In addition to the differences in sample and stacking algorithm, another source

of this discrepancy may be the exclusion of X-ray detected sources (AGN) in the present work.

LESS 870 μm . Submillimeter data at 870 μm were obtained from the Large Apex Bolometer Camera ECDF-S Submillimeter Survey (LESS) (Weiss et al. 2009), which reaches a 1σ depth of approximately $1.2 \text{ mJy beam}^{-1}$. The LESS catalog contains 126 individually detected submillimeter sources (Weiss et al. 2009) and these data have been used previously for stacking analyses of BzK galaxies (Greve et al. 2010).

K band sBzK positions are compared to the 870 μm catalog to determine individual detections. In 870 μm data, in redshift bins from $0.9 < z \leq 1.2$, $1.2 < z \leq 1.5$, $1.5 < z \leq 2.0$ and $2.0 < z \leq 3.2$, there are 1, 3, 12, 5 individual detections and 49, 155, 218, 147 stacked positions, respectively. The simultaneous stacking and deblending algorithm discussed above is used to stack positions in the final, LESS beam smoothed flux map (Weiss et al. 2009). All galaxies in the MUSYC K band catalog are used in the deblending calculations. Individual detections and the stacking detections are combined into a single average signal for each redshift bin, as discussed above and in Section 7. We find significant stacking detections in all but the lowest redshift bin, see Table 3. An average detection for the entire sample, $0.9 < z \leq 3.2$, yields $0.49 \pm 0.05 \text{ mJy}$ (SNR=10), consistent with the results of Greve et al. (2010) for a nearly identical set of galaxies in the same field.

Radio. Radio data at 610 MHz were obtained from the Giant Metrewave Radio Telescope (GMRT) survey of the ECDF-S, which reaches a typical depth of $40 \mu\text{Jy beam}^{-1}$ (Ivison et al. 2010a). 1.4 GHz data were obtained from the Very Large Array (VLA) survey, which covers the ECDF-S to a typical depth of $8 \mu\text{Jy beam}^{-1}$ and includes 464 cataloged sources (Miller et al. 2008). In the radio regime we adopted the technique of Ivison et al. (2007) - dividing the catalog into the same redshift bins used earlier. Median images are made from the VLA and GMRT stacks, to reduce the influence of

radio-loud AGN. In the radio regime, where the spatial resolution is relatively high, making images allows us to conserve flux density that would otherwise be lost due to smearing by astrometric uncertainties and finite bandwidth (chromatic aberration) at the cost of larger flux density uncertainties. Total flux densities are measured within *AIPS* using Gaussian fits over 9×9 -pixel regions; we determine the appropriate source centroid by making radio stacks using every available sBzK galaxy, then use this centroid to minimize flux density uncertainties and avoid spurious fits; at 1.4 GHz, where both forms of smearing are most prevalent, flux densities are 1.37 and $1.55\times$ higher than the peak values at 610 MHz and 1.4 GHz, respectively. Such losses are not expected where the astrometry is accurate to a small fraction of a beam, as it is in far-IR and submillimeter regimes. Radio fluxes are indicated in Table 3 and discussed below.

4. Estimating Luminosity and Star Formation Rates

The multiwavelength, stacked flux densities discussed in Section 3 are used to form spectral energy distributions (SEDs) for the sBzK galaxies in our four redshift bins. In particular, the IR-submillimeter SEDs are used to estimate IR luminosity and the corresponding SFR for each bin. To compare different SFR calibrations, we also compute UV, X-ray and radio luminosities from these data.

4.1. IR Luminosity and SFR Estimation

In order to estimate L_{IR} , we fit observed IR photometry to template libraries from Chary & Elbaz (2001), hereafter CE01. These templates are based on the stellar population synthesis models of Silva et al. (1998), which employ Simple Stellar Populations (SSP) of varying age and metallicity and include enrichment of the interstellar medium by outflows

from Asymptotic Giant Branch (AGB) stars. The templates are formed by interpolation of the SEDs of several prototypical galaxies in the local universe representing luminosity classes of normal galaxies (M51), starburst galaxies (M82), luminous infrared galaxies, LIRGs (NGC 6090), and ultraluminous infrared galaxies, ULIRGs (Arp 220). Template SEDs are generated in the range 0.1-1000 μm ; however, the optical-NIR spectral regions of the templates are considered to be highly uncertain. Other templates are adopted in the literature (Dale & Helou 2002; Lagache et al. 2003; Siebenmorgen & Krügel 2007); succinct descriptions of these various template libraries and comparisons between them can be found in Symeonidis et al. (2008).

Estimation of L_{IR} from IR data has often been complicated by the availability of only a single IR photometric measurement, most commonly observed frame 24 μm , thereby making the resulting fits highly uncertain. For high redshift systems, observed frame 24 μm corresponds to a rest frame wavelength regime dominated by spectral emission features of Polycyclic Aromatic Hydrocarbons (PAHs) and hot dust from AGN and silicate absorption. PAHs are honeycombed, carbon ring molecules that reprocess UV starlight and give rise to ubiquitous mid-IR spectral lines observed in many astrophysical systems (Tielens 2008); however, these features are not necessarily ideal proxies for star formation in the local universe (Peeters et al. 2004), and they further complicate SED fitting of high redshift systems.

In this investigation, we explore several approaches to fitting the IR-radio data to CE01 templates to determine L_{IR} . In each case, a region of the IR-radio spectrum is chosen for template fitting. Fits are performed on each photometric redshift bin averaged spectrum. The template rest frame luminosity is converted to an observed frame flux distribution at the median redshift of the redshift bin. Then the observed frame model flux distribution is convolved with each photometric bandpass transmission function to generate predicted

model photometry. The predicted photometry is combined with observed photometric fluxes and errors to generate a χ^2 statistic for each fit. Each template in the library is fit in this way, with the smallest χ^2 fit chosen as the best fit template. For fits that include observations at multiple wavelengths, an overall normalization, A , set to its analytical best fit value via $\partial\chi^2/\partial A = 0$, is factored into the best fit spectrum and then variations in χ^2 space are used to determine confidence intervals for the subsequent L_{IR} estimate. To compare the multiwavelength approach to a single band L_{IR} estimate, we also perform fits to the 24 μm data alone. For these single band fits, there is no free normalization factor, and the CE01 template luminosity is used directly to estimate L_{IR} . For the single band fits, the variation of χ^2 with template index is used as the basis for determining confidence intervals; 68% error bars are found for the L_{IR} estimate, and these errors are propagated into an SFR uncertainty. We explore several additional approaches to estimating L_{IR} from the data using CE01 template fits: For each redshift bin, we fit (i) the entire optical through radio data, (ii) the 24 μm and longer wavelength data, (iii) the long wavelength IR and radio data excluding 24 μm , (iv) only the submillimeter data near the peak of the dust emission spectrum, and (v) the IR data excluding the radio data. We also fit models of gray body emission. Some of these fits are illustrated in Table 4 and Figure 4 and are discussed in Section 5.

We use the calibration of Kennicutt (1998) to convert L_{IR} to estimated star formation rate. This calibration assumes a continuous burst of age 10-100 Myr and relates the L_{IR} integrated from 8-1000 μm to star formation rate according to

$$SFR_{IR}(M_{\odot} \text{ yr}^{-1}) = 4.5 \times 10^{-44} L_{IR}(\text{erg s}^{-1}) \quad (2)$$

SFR estimates for our redshift binned sBzKs are discussed in Section 5.

4.2. UV Continuum Luminosity and SFR Estimation

According to the calibration of Kennicutt (1998), star formation rate is related to the UV (1500 Å) specific luminosity, L_ν , as:

$$SFR_{UV}(M_\odot \text{ yr}^{-1}) = 1.4 \times 10^{-28} L_\nu(\text{erg s}^{-1} \text{ Hz}^{-1}) \quad (3)$$

We apply this expression to luminosities, L_ν^{Uncorr} , that are uncorrected for dust attenuation, to estimate the contribution to star formation rate that is unobscured by dust. To determine L_ν^{Uncorr} for each stacked, redshift binned set, using the available optical-NIR photometry, we estimate the restframe 1570 Å flux density via interpolation of the two bracketing broad band fluxes. The specific luminosity, L_ν^{Uncorr} , at the bin median redshift, z , is then found from the flux density, f_ν^{Uncorr} and the luminosity distance, D_L , according to

$$L_\nu^{Uncorr}(\text{erg s}^{-1} \text{ Hz}^{-1}) = 1 \times 10^{-29} f_\nu^{Uncorr}(\mu\text{Jy}) \frac{4\pi D_L^2}{(1+z)}. \quad (4)$$

Unobscured star formation rates for our redshift binned sample of galaxies are summarized in Table 5. Due to partial absorption of UV radiation by dust, which re-radiates the emission in the IR, these estimates of unobscured star formation are only a small component of the total star formation rate at each redshift bin.

Dust absorption also causes reddening of the spectrum since shorter wavelengths are preferentially absorbed. As a result, it is reasonable that dust radiation, estimated as L_{IR}/L_{UV} , is found to be correlated with the UV spectral index, β , where $f_\lambda \propto \lambda^\beta$ with 0.4 dex scatter when calibrated against starburst galaxies in the local universe (Meurer et al. 1999). This relationship is subsequently used to attempt to correct UV star formation rate estimates for dust attenuation in high redshift LBGs, e.g. (Meurer et al. 1999; Adelberger & Steidel 2000; Reddy et al. 2010), BzK galaxies (Daddi et al. 2007b), and galaxies at lower redshift, e.g. (Buat et al. 2010; Howell et al. 2010; Takeuchi et al. 2010).

In order to compute this dust correction, we fit the rest frame UV f_λ spectrum to a

power law: $f_\lambda(\lambda) = A\lambda^\beta$. A range of trial β values are used $-2.5 < \beta < 1.0$ in steps $\Delta\beta = 0.01$. The wavelength range of the fits, $[1268, 2580]$ Å in the rest frame, are chosen to be the same as that used in Calzetti et al. (1994). These values are redshifted into the observed frame, and photometry data falling within this range are used for the fits. For each trial value of β , predicted flux values are computed at each relevant, observed wavelength by integrating over the filter bandpass transmission function, $T(\lambda)$, and IGM absorption function, $M(\lambda)$, from Madau (1995). The integral is expressed in terms of the number of photons detected, hence an extra factor of λ is included in the integrand, as illustrated below in Equation 5. The integral is normalized to units of μJy by dividing by the corresponding integral of a flat in f_ν reference spectrum ($f_\nu^{ref}=1 \mu\text{Jy}$), which is converted to a photon number spectrum. This approach leads to the expression for predicted flux density, $f_{\nu_i}^{pred}$, for each broadband filter, i

$$f_{\nu_i}^{pred}(\mu\text{Jy}) = A \frac{\int \lambda^\beta T_i(\lambda) M(\lambda) \lambda d\lambda}{\int f_\lambda^{ref}(\lambda) T(\lambda) \lambda d\lambda} \quad (5)$$

The statistic X^2 is formed as a summation over the observed photometric data, $f_{\nu_i}^{obs}$, with errors, σ_i^{obs} , taken from the data.³

$$X^2 = \sum_i \left(\frac{f_{\nu_i}^{obs} - f_{\nu_i}^{pred}}{\sigma_i^{obs}} \right)^2 \quad (6)$$

We optimize the normalization parameter, A , by selecting the value for which $\partial X^2 / \partial A = 0$. Finally the complete, normalized predicted flux in μJy is computed from Equation 5. The above fit procedure is repeated for each trial β value, and the fit with the smallest X^2 is chosen to represent the data.

The resulting power law index, β , is then used to compute the UV extinction from the

³since each observed flux value is a weighted average of many observations, the observed errors are very small; due to systematics in the photometry, the resulting X^2 values are very large compared to a χ^2 statistic

empirical relation of Meurer et al. (1999)

$$A_{1600} = 4.43 + 1.99\beta, \quad (7)$$

which is found to have 0.55 mag dispersion about their fit in A_{1600} and a standard error in the fit zero point of 0.08 mag; see Equation (11) and Figure 1 from Meurer et al. (1999). Implicit within the derivation of this widely used relation is the quantity $IRX \equiv F_{IR}/F_{UV}$, the ratio of integrated IR to UV flux. F_{IR} and F_{UV} are defined relative to bandpasses measured with the *Infrared Astronomy Satellite (IRAS)* and *International Ultraviolet Explorer (IUE)*, whose observations provided the data for their study. As discussed in Section 5, these definitions may have implications for interpreting this relationship more generally. The UV extinction is then used to correct the measured UV flux according to

$$F_{UV}^{Corr} = 10^{0.4A_{1600}} F_{UV}^{Uncorr} \quad (8)$$

Finally the corrected UV flux is used to estimate the star formation rate using Equation 3.

The above procedure is executed for each of the redshift binned sBzK photometry data sets. The results of these computations are shown in Table 5 and discussed in Section 5. Errors to the UV and corrected UV SFR estimates are computed with standard error analysis, including two terms: flux estimate error and photometric redshift error. The flux estimate error is derived from the observed photometry and is computed along with the interpolated S_{1570} , the flux at 1570\AA . For the redshift error, we adopt the value of $\delta z/(1+z) = 0.009$ (Cardamone et al. 2010). We propagate this error into the luminosity distance and the resulting estimate of the luminosity.

4.3. Radio Luminosity and SFR Estimation

Our data include flux measurements, S_ν , at 1.4 GHz and 610 MHz for each of the redshift binned spectral energy distributions; we estimate the radio spectral index, $S_\nu \propto \nu^\alpha$,

(typical $\alpha \sim -0.8$ for star forming galaxies) from these two measurements. Radio fluxes and their derived quantities are tabulated in Table 6. In estimating SFR from the radio data, we use the flux estimates obtained from median stacking of galaxies in each of the redshift bins to obtain results that are robust against radio bright outliers caused by radio lobes from recent AGN activity that X rays will not always detect. We use the median redshift, z , and the corresponding luminosity distance D_L in Mpc to compute the aggregate rest frame 1.4 GHz luminosity, $L_{\nu,1.4GHz}$ from the observed frame 1.4 GHz flux, S_{ν} , according to

$$L_{\nu,1.4GHz}(W \text{ Hz}^{-1}) = 9.523 \times 10^{12} \frac{4\pi D_L^2}{(1+z)^{1+\alpha}} S_{\nu,1.4GHz}(\mu Jy) \quad (9)$$

We assume here that the distribution of galaxies in flux is independent of redshift across a bin. This assumption would be violated in the case of source evolution within a bin, so the subsequent SFR estimates should be interpreted with some caution. To estimate star formation rate from $L_{\nu,1.4GHz}$, we use the model of Condon (1992) as implemented in Haarsma et al. (2000) and Dunne et al. (2009) with the exception that we use spectral indices, α , determined from the data rather than using the typical value of $\alpha = -0.8$. Following the implementation in Haarsma et al. (2000), SFR is a function of $L_{\nu,1.4GHz}$, scaled by a factor Q and is given by

$$SFR_{1.4GHz}^{Condon}(M_{\odot} \text{ yr}^{-1}) = Q \frac{L_{\nu}^{1.4GHz}(W \text{ Hz}^{-1})}{5.3 \times 10^{21} \nu^{\alpha}(GHz) + 5.5 \times 10^{20} \nu^{-0.1}(GHz)} \quad (10)$$

We use the value $Q=5.5$ to scale the $SFR(M>5 M_{\odot})$ calculated in Condon (1992) to $SFR(0.1-100 M_{\odot})$ used here; this scaling factor depends on the assumed (Salpeter) IMF used here and in Condon (1992).

For comparison, we also estimate SFR from 1.4 GHz flux using the calibration of Bell (2003). This calibration assumes that nonthermal radio emission directly tracks the SFR, is based on the IR-radio correlation, and is chosen so the radio SFR matches the IR SFR for $L \geq L^*$ galaxies. The discussion in Bell (2003) of suppression of non-thermal radio emission

for low-luminosity ($L < 6.4 \times 10^{21} \text{ W Hz}^{-1}$) galaxies does not apply to our sample of high luminosity sBzK galaxies. Accordingly, the SFR calibration

$$SFR_{1.4GHz}^{Bell}(M_{\odot} \text{ yr}^{-1}) = 5.52 \times 10^{-22} L_{1.4GHz} \quad (11)$$

is adopted here. A similar calibration is found in Yun et al. (2001). $SFR_{1.4GHz}^{Condon}$ exceeds $SFR_{1.4GHz}^{Bell}$ by a factor of two; the calibration of Condon (1992) explicitly models the thermal and nonthermal emission mechanisms, whereas the calibration of Bell (2003) relies upon the IR-Radio correlation. Thus we expect agreement between $SFR_{1.4GHz}^{Bell}$ and IR based SFR estimates, if the IR-radio correlation continues to hold at high redshift, as has indeed been suggested by recent *Herschel Space Observatory* observations (Ivison et al. 2010b).

Error analysis is performed incorporating uncertainties from redshift, spectral index, and flux measurement. When only flux measurement uncertainties are included in the error budget, SFR uncertainties agree to within 30% of published values (Dunne et al. 2009). However, when redshift uncertainties and spectral index estimate uncertainties are included, the total SFR uncertainties are substantially larger than previously reported values.

4.4. X-Ray Luminosity and SFR Estimation

X-ray luminosity is used as a calibration for SFR based on empirical correlations between X-ray luminosity and radio (Bauer et al. 2002) and FIR luminosity (Ranalli et al. 2003) in normal (non AGN or ULIRG) local ($z \lesssim 0.1$) star forming galaxies with low to moderate SFR ($\lesssim 100 M_{\odot} \text{ yr}^{-1}$). The observed correlation between X-ray and FIR luminosity over three orders of magnitude in X-ray luminosity with a scatter of 0.27 (0.3) dex for soft band (hard band) X-ray luminosities lead to the calibrations of Ranalli et al. (2003),

$$SFR_{0.5-2keV}^{Ranalli}(M_{\odot} \text{ yr}^{-1}) = 2.2 \times 10^{-40} L_{0.5-2keV}(\text{erg s}^{-1}) \quad (12)$$

$$SFR_{2-10keV}^{Ranalli}(M_{\odot} \text{ yr}^{-1}) = 2.0 \times 10^{-40} L_{2-10keV}(\text{erg s}^{-1}). \quad (13)$$

These calibrations extend over the range 0.1 - 100 $M_{\odot} \text{ yr}^{-1}$, and are implicitly based upon the IR SFR calibration of Kennicutt (1998) which assumes a Salpeter IMF and 0.1-100 M_{\odot} mass range consistent with other calibrations mentioned in this paper.⁴

Theoretically motivated investigations of the sources of X-ray emission in star forming galaxies lead to independent X-ray SFR calibrations (Persic & Rephaeli 2002; Grimm et al. 2003; Gilfanov et al. 2004). X-ray sources in star forming galaxies include HMXBs and LMXBs in varying fractions, and to a lesser extent SNRs. Based upon X-ray spectral decomposition of nearby star forming galaxies, Persic et al. (2004) derive an SFR calibration based upon the luminosity of HMXBs, which are the dominant tracer of star formation in X rays. This calibration is

$$SFR_{2-10keV}^{Persic}(M_{\odot} \text{ yr}^{-1}) = 10^{-39} L_{2-10keV}^{HMXB}(\text{erg s}^{-1}) \quad (14)$$

Applying this calibration more generally depends upon assumptions for the fraction, f , of HMXB X-ray luminosity to total X-ray luminosity. From X-ray spectral modeling, Persic et al. (2004) estimated this fraction as $f \sim 0.2$ (with substantial scatter due to low statistics) for their sample of nearby star forming galaxies, $f \sim 0.1$ for AGN dominated ULIRGs, and $f \sim 1$ for non-AGN dominated ULIRGs. For their high redshift ($z \sim 1$) sub-sample of galaxies, lacking spectral information, the assumption $f \sim 1$ is theoretically motivated (LMXBs do not have time to form over the ~ 6 Gyr lifetime of a galaxy at $z \sim 1$) and brings X-ray SFRs into agreement with radio based SFRs and averaged [OII] emission line based SFRs for their sample.

⁴Note that the radio SFR calibration cited in Ranalli et al. (2003) refers to $M > 5 M_{\odot}$ mass range. For a Salpeter IMF, the resulting SFRs differ by a factor of 5.5 from the 0.1-100 M_{\odot} range used here.

Thus for nearby star forming galaxies, $f = 0.2$, and $L_{2-10\text{keV}}^{HMXB} = 0.2 L_{2-10\text{keV}}^{Total}$, which brings the calibration of Persic et al. (2004) into equivalence with the calibration of Ranalli et al. (2003). The data for high redshift galaxies do not directly constrain the HMXB luminosity fraction; for the plausible assumption $f = 1$ and $L_{2-10\text{keV}}^{HMXB} = L_{2-10\text{keV}}^{Total}$, then the SFRs estimated from Persic et al. (2004) exceed those of Ranalli et al. (2003) by a factor of 5. Under these circumstances, we adopt the X-ray calibration of Persic et al. (2004) with $f \sim 1$ for sBzKs.

Luminosity estimates for our sBzK galaxies in each photometric redshift bin are obtained from stacked X-ray fluxes, using the median redshifts. The observed frame soft band and hard band fluxes are converted to the rest-frame assuming a spectrum with photon index $\Gamma=1.2$ and cut off energy, $E_c=20$ keV. X-ray fluxes, luminosities and SFRs are tabulated in Table 2 and discussed in Section 5.

4.5. Simulations

The approach to stacking presented here consists of combining galaxies in bins of photometric redshift, in order to study star formation in sBzK galaxies over cosmic time. Averaging the photometric flux density from galaxies at slightly different redshifts introduces redshift smearing. In order to study this effect, we simulate a set of identical CE01 template spectral models. These spectra are shifted to the identical redshifts of galaxies in our $1.5 < z \leq 2.0$ redshift bin, and then averaged together, analogous to the actual stacking procedure. The redshift bin averaged spectrum is nearly identical to the template spectrum except for moderate smearing of the emission peaks that contributed a negligible amount to the integral; consequently, the quantity of interest, the integrated IR luminosity, is robust against redshift smearing over our bin widths.

Of greater concern is the effect on L_{IR} due to photometric redshift errors. To quantify the contribution of these errors to the estimated L_{IR} for each redshift bin, we simulate a set of identical CE01 template sources, with spectra equal to the best fit spectrum. These sources are distributed in redshift to simulate the observed source distribution and to account for photometric redshift errors. The photometric redshift error distribution is determined from comparison of spectroscopic and photometric redshifts for the subset of sources with both estimates available and is shown in Figure 3. This distribution is well fit by a Gaussian with mean = -0.021 (i.e. bias) and $\sigma=0.081$ (i.e. scatter). The bias is first removed from the simulated object redshifts, and then artificial redshift errors drawn from this biased, Gaussian distribution are added in each repeated trial of the simulation. The resulting spectra are averaged, and this averaged spectrum is integrated to determine L_{IR} . An example of these spectra from the $1.5 < z \leq 2.0$ redshift bin simulation is illustrated in Figure 5. From the figure, it is apparent that the averaged spectrum has a slightly higher flux than the single object spectrum near the emission peak and therefore will overestimate L_{IR} . For each repeated trial, the fractional error in the L_{IR} estimate is determined by comparing the bin averaged L_{IR} to the corresponding quantity determined from integrating the single CE01 template at the bin median redshift. The frequency distribution of L_{IR} fractional errors is determined directly from 10^3 repeated trials for each redshift bin. The fractional error distributions for redshift bins $0.9 < z \leq 1.2$, $1.2 < z \leq 1.5$, $1.5 < z \leq 2.0$ and $2.0 < z \leq 3.2$ are each Gaussian with mean = 16%, 10%, 14%, 5% and $\sigma = 7\%$, 3%, 3%, 3% respectively. The fractional error distribution for the $1.5 < z \leq 2.0$ bin is illustrated in Figure 5.

5. Results

5.1. IR SFR Estimates

SFR_{IR} values are obtained from CE01 template fits to determine the integrated IR luminosity. We tried various approaches to fitting the IR-radio data to CE01 and gray body templates, as illustrated in Figure 4 and Table 4. The low redshift bin, $0.9 < z \leq 1.2$, suffers from lack of detections in the BLAST sub-millimeter bands (upper 1σ error bars are shown in the figure). Data in the highest redshift bin, $2.0 < z \leq 3.2$, also suffer from weak sub-millimeter detections, leading to large error bars and poor fits to the CE01 templates. Redshift binned spectra in the range $1.2 < z \leq 1.5$ and $1.5 < z \leq 2.0$ include significant submillimeter detections in BLAST and LESS bands. Formally acceptable χ^2 (defined as probability ~ 0.5) are found for the $1.2 < z \leq 1.5$ bin with a fit to the $\lambda > 24 \mu\text{m}$ data. This fit also roughly matches the optical/NIR data that is excluded from the optimization. In general, optical/NIR data are excluded from the fits to CE01 templates because the templates are considered to be incomplete for $\lambda < 1\mu\text{m}$.

For comparison with a complementary method of L_{IR} estimation, each plot of Figure 4 illustrates fits of the submillimeter peak (70-870 μm data only) to a gray body spectrum, $S_\nu \propto \nu^\beta B(\nu, T)$ where the emissivity index, $\beta = 1.5$, and $B(\nu, T)$ is the Planck function. For the redshift range $0.9 < z \leq 1.2$, the temperature is fixed at 50 K, which gives a better visual fit to the emission peak than lower temperatures used in other redshift bins, and only the normalization is allowed to vary. For the redshift range $1.2 < z \leq 1.5$ (second row from the top), the gray body fit has χ^2 and L_{IR} values similar to the best fit CE01 template; the best fit temperature is 41 ± 5 K. The gray body fit to the next highest redshift bin, $1.5 < z \leq 2.0$, yields a dust temperature of 43 ± 5 K. For the redshift range $2.0 < z \leq 3.2$, the temperature is fixed at 40 K and the normalization is allowed to vary.

The SFR_{IR} values in Table 7 are obtained from L_{IR} estimates from fits of MIR-radio ($\lambda \geq 24\mu\text{m}$) photometry to CE01 templates. We find excellent agreement between SFR_{UV}^{Corr} and SFR_{IR+UV} in the lower redshift bins, and a slight discrepancy, as SFR_{UV}^{Corr} exceeded SFR_{IR+UV} in the higher redshift bins. Our flux limited data sampled more luminous galaxies in the higher redshift bins ($L_{IR} \approx 6 \times 10^{10} L_{\odot}$ at $0.9 < z \leq 1.2$, vs. $L_{IR} \approx 7 \times 10^{11} L_{\odot}$ at $2.0 < z \leq 3.2$, see Table 4). This overestimate of SFR_{UV}^{Corr} compared to SFR_{IR+UV} is similar to findings in $250\mu\text{m}$ selected LIRGs at intermediate redshifts (Buat et al. 2010); however, LIRGs in the local universe appear not to exhibit this trend (Buat et al. 2007; Takeuchi et al. 2010; Howell et al. 2010). Discrepancies between SFR_{UV}^{Corr} and SFR_{IR+UV} may have arisen at least in part because the commonly used Meurer et al. (1999) dust attenuation correction, implemented in Equation 7, is derived from the estimate of integrated IR flux from IRAS observations used in Helou et al. (1988), which assumes a 50-100 K blackbody spectrum (notably our gray body fits to binned spectra yield slightly lower temperatures of 41 K and 43 K) to convert IRAS $60\mu\text{m}$ and $100\mu\text{m}$ observations into integrated IR fluxes.

Table 7 also illustrates SFR_{IR} estimated from fitting only the $24\mu\text{m}$ data to CE01 templates. The resulting poor fit to the data in the highest redshift bin, $2.0 < z \leq 3.2$, illustrated in Figure 4 (discussed below), overestimates L_{IR} by approximately a factor of 6; overestimation of L_{IR} by this same factor is reported by Muzzin et al. (2010) based on analysis of single galaxies detected from MIR through submillimeter wavebands. Overestimation of L_{IR} explains the discrepancy between SFR_{UV}^{Corr} and SFR_{IR+UV} that has been reported previously when L_{IR} is determined from a single $24\mu\text{m}$ observation (Daddi et al. 2007b; Papovich et al. 2007; Murphy et al. 2009; Muzzin et al. 2010). PAH features near $24\mu\text{m}$ in the observed frame distort the fit when only $24\mu\text{m}$ data are used. As a result, we find that $24\mu\text{m}$ only based SFR estimates should be interpreted with great caution and avoided at $z > 2$.

Various other methods of estimating integrated IR flux and luminosity from one or several IR band observations are explored in the literature (Takeuchi et al. 2005; Symeonidis et al. 2008). However, the results of this study illustrate the hazards of estimating integrated IR values from single band data. The observed deviations in the Meurer et al (1999) relation among LIRGs and ULIRGs in high redshift galaxies, and the scatter in this relation generally, may arise at least in part from inaccuracies of measuring integrated IR flux. Alternatively, UV properties of these populations may be strongly variable, as observed in the local universe. A larger, systematic and panchromatic study of LIRGs and ULIRGs at high redshift is needed to better understand these issues.

5.2. UV SFR Estimates

As discussed in Section 4.2, the Meurer et al. (1999) relation between L_{IR}/L_{UV} and UV spectral index, β , is used to estimate and correct for dust attenuation, particularly when IR data are unavailable. However, normal star forming galaxies in the local universe are found to deviate from this relation (e.g. Boissier et al. 2007; Buat et al. 2010). Thus it is important to measure L_{IR}/L_{UV} independently as a check on its application in high redshift systems.

To estimate L_{IR}/L_{UV} for our redshift binned sBzKs, we use values of L_{IR} and L_{UV} discussed above. Specific UV luminosity values, L_{UV} , in units of $10^{28} \text{ erg s}^{-1} \text{ Hz}^{-1}$ are taken from Table 5, and converted to luminosity by multiplying by the frequency $\nu = 1.8 \times 10^{15} \text{ Hz}$ (rest frame 1600 \AA), and then converted to units of $10^{11} L_{\odot}$. L_{IR} estimates, obtained from fits of mid-IR through radio photometry ($\lambda \geq 24 \mu\text{m}$) to CE01 templates, are taken from Table 4. The resulting L_{IR}/L_{UV} ratios are 14.8, 35.2, 27.8, 18.3 for the redshift bins $0.9 < z \leq 1.2$, $1.2 < z \leq 1.5$, $1.5 < z \leq 2.0$ and $2.0 < z \leq 3.2$ respectively. β values for each redshift bin are taken from Table 5. These data are plotted as $\log(L_{IR}/L_{UV})$ vs. β in Figure 6. These redshift bin averaged sBzK values can be compared to similar data for individual,

IR selected systems including starburst and star forming galaxies at lower redshift ($z < 0.3$) reported in Buat et al. (2010); data for these low redshift systems are indicated as points in Figure 6 ⁵. The $L_{IR}/L_{UV} - \beta$ relation for normal star forming galaxies in the local universe reported by Boissier et al. (2007) is indicated by the dashed, cyan curve in the figure.

Figure 6 indicates that our redshift binned sBzK estimates match the Meurer et al. (1999) relation, and this agreement gives confidence in the UV corrected SFR estimates. The Meurer et al. (1999) relation is essentially equivalent to the dust attenuation law of Calzetti et al. (1994). The overall success of the Meurer et al. (1999) relation then implies that the average sBzK dust attenuation is consistent with the model of Calzetti et al. (1994).

Figure 6 also suggests that high redshift BzK galaxies are a different population than normal star forming galaxies in the local universe. For a given IR luminosity, these systems have on average a bluer UV spectrum than normal star forming galaxies in the local universe, indicative of a younger stellar population and/or diminished dust obscuration due to a modified dust attenuation law.

A summary of estimated star formation rates for the redshift binned sBzK galaxies are illustrated in Table 7. The uncorrected UV SFRs, hereafter SFR_{UV} , are only a small fraction of other estimates, indicating that dust obscuration is significant in these systems. Dust corrected UV SFRs, SFR_{UV}^{Corr} , are in the range 15-180 $M_{\odot} \text{ yr}^{-1}$, an order of magnitude greater than the SFR_{UV} at all redshifts, and somewhat lower than has been reported

⁵Data from these nearby systems include β values that are estimated from *Galaxy Evolution Explorer* (GALEX) FUV and NUV measurements. We use the empirical calibration of Kong et al. (2004) to transform these β values to be consistent with β estimates obtained from the method of Calzetti et al. (1994) and used in this paper.

previously for sBzKs, e.g. $\sim 200 \text{ M}_{\odot} \text{ yr}^{-1}$ for GOODS-N (Daddi et al. 2005). These dust corrected UV SFRs can be compared to the total SFR derived from uncorrected UV and IR estimates, $\text{SFR}_{IR+UV} \equiv \text{SFR}_{IR} + \text{SFR}_{UV}$, as discussed below.

5.3. Radio SFR Estimates

Radio fluxes, luminosities, spectral indices and associated star formation rates are reported in Table 6 and star formation rates are compared to calibrations in other wavebands in Table 7. Upper limits are found in both radio bands in the $0.9 < z \leq 1.2$ redshift bin. The radio spectral indices, determined from 610 MHz and 1.4 GHz data in the $1.2 < z \leq 1.5$ and $2.0 < z \leq 3.2$ redshift bins are -0.66 ± 0.34 and -0.84 ± 0.47 , consistent with the value of -0.8 typically observed in star forming galaxies. The radio spectral index in the $1.5 < z \leq 2.0$ bin is unusually steep, -1.37 ± 0.41 , due to the unexpectedly high flux in the 610 MHz band; this high flux estimate is propagated to an unexpectedly high star formation rate in one radio calibration, as discussed below, but otherwise the observations at other wavelengths for this redshift bin are unremarkable.

The radio based SFR estimates from the calibration of Condon (1992) and Bell (2003) are compared in Table 6. It has been reported previously that $\text{SFR}_{1.4\text{GHz}}^{\text{Condon}}$ exceeds $\text{SFR}_{1.4\text{GHz}}^{\text{Bell}}$ by approximately a factor of two (Bell 2003). $\text{SFR}_{1.4\text{GHz}}^{\text{Condon}}$ incorporates separately the effects of synchrotron radiation and thermal free-free emission, whereas $\text{SFR}_{1.4\text{GHz}}^{\text{Bell}}$ is an empirical correlation that uses the IR-Radio correlation. Discrepancies between the radio SFR calibrations of Bell (2003) and Condon (1992) are not entirely surprising given the different assumptions of each calibration.

$\text{SFR}_{1.4\text{GHz}}^{\text{Condon}}$ can be compared to previous reported results for stacking sBzKs; in stacking a $K_{AB} \leq 23$ sample of BzKs, Dunne et al. (2009) reported a median sBzK luminosity of

$1.28 \times 10^{23} \text{ W Hz}^{-1}$ corresponding to $\text{SFR}=154\pm7 \text{ M}_{\odot} \text{ yr}^{-1}$, which is consistent with our $1.2 < z \leq 1.5$ bin result of $139\pm32 \text{ M}_{\odot} \text{ yr}^{-1}$, but lower than our higher redshift bin results by a factor of ~ 3 . However, as mentioned in Section 5.6, the sample of BzKs reported in Dunne et al. (2009), which is taken from the catalog of Lane et al. (2007), may have been contaminated by low redshift interlopers.

The values of $\text{SFR}_{1.4\text{GHz}}^{\text{Bell}}$ indicated in Table 6 are consistent with UV, IR and X-ray based calibrations presented here. The values presented here are closer to but somewhat larger than results from the COSMOS survey; Pannella et al. (2009) reported radio based SFR estimates in the range $30\text{-}100 \text{ M}_{\odot}\text{yr}^{-1}$ (see their Figure 3; SFR plotted vs B magnitude) for BzKs using the empirical IR-Radio based calibration of Yun et al. (2001).

5.4. X-ray SFR Estimates

X-ray based SFRs are also indicated in Table 7. In the soft band, the $\text{SFR}_{0.5-2\text{keV}}^{\text{Ranalli}}$ estimates (not shown in the table) for each photometric redshift bin are <2 (3σ upper limit), 2 ± 0.3 , 6 ± 1 , $14 \pm 2 \text{ M}_{\odot} \text{ yr}^{-1}$ in redshift bins $0.9 < z \leq 1.2$, $1.2 < z \leq 1.5$, $1.5 < z \leq 2.0$ and $2.0 < z \leq 3.2$ respectively. These soft band luminosity and SFR estimates appear to be depressed because of intrinsic absorption. Average HI column density is estimated to be $N_H \sim 10^{22} \text{ cm}^{-2}$ from the IR and radio SFR using the Schmidt-Kennicutt law (Kennicutt 1998) to estimate gas density, assuming a 6 kpc BzK radius (Genzel et al. 2006). For roughly solar metallicity, even a factor of a few lower observed N_H would cause soft band luminosity to significantly underestimate SFR. The hard band luminosities are unaffected by intrinsic absorption at these column densities. The corresponding SFR estimates for each photometric redshift bin, according to calibrations of Ranalli et al. (2003) and Persic et al. (2004) are indicated in Table 7. Based upon the findings of Persic et al. (2004) for $z \sim 1$ galaxies, as compared to nearby star forming galaxies discussed in Section 4.4,

$\text{SFR}_{2-10\text{keV}}^{\text{Persic}}$ may be the preferred X-ray based estimate. As indicated by Table 7, these values agree with $\text{SFR}_{UV}^{\text{Corr}}$, $\text{SFR}_{1.4\text{GHz}}^{\text{Bell}}$ and SFR_{IR+UV} to within error bars for all but the largest redshift bin. Overluminous X-ray luminosity leading to the large SFR estimate in the highest redshift bin may indicate residual contamination from heavily obscured AGN at these redshifts, in which case our stacking results indicate an average luminosity of 5.4×10^{40} erg s⁻¹ in the range $2.0 < z \leq 3.2$.

The discrepancies between SFR calibrations of Persic et al. (2004) and Ranalli et al. (2003) are understood by considering the different methods of each calibration and the galaxy samples upon which they are derived. The calibration of Ranalli et al. (2003) is based upon an empirical IR–X-Ray correlation of relatively low luminosity star forming galaxies in the local universe. As reported by Persic et al. (2004), X-ray spectral decomposition of the systems in Ranalli et al. (2003) shows an HMXB luminosity fraction, $f \sim 0.2$, with the remainder of the X-ray emission coming from long lived, LMXBs. With this HMXB luminosity fraction, the calibration of Persic et al. (2004) is consistent with that of Ranalli et al. (2003) when applied to the same sample of low luminosity, star forming galaxies. At high redshifts, the calibration depends upon an assumed HMXB luminosity fraction and therefore has this additional uncertainty compared to calibrations in other wavebands.

5.5. Comparison of SFR Estimates

SFR estimates from X-ray through radio calibrations are compared in Table 7. To gauge their consistency, we plot the ratio of SFR computed from each calibration to SFR_{IR+UV} in Figure 7. In this figure, $\text{SFR}_{IR}/\text{SFR}_{IR+UV}$ is most nearly equal to one, reflecting the importance of IR luminosity in estimating SFR for sBzK galaxies compared to uncorrected UV luminosity. $\text{SFR}_{UV}^{\text{Corr}}$ is consistent with SFR_{IR+UV} to within a factor of two over our redshift range, indicating success for the dust correction method of Meurer

et al. (1999) for sBzKs. Comparing $\text{SFR}_{24\mu m}$ to SFR_{IR+UV} in Figure 7 illustrates the overestimate of SFR at high redshift from this single band estimate of IR luminosity, as discussed in Section 5.1.

Among radio based SFR estimates, Figure 7 illustrates agreement between $\text{SFR}_{1.4GHz}^{Bell}$ and SFR_{IR+UV} to within a factor of two over our redshift range; however, this agreement is a consequence of the IR-Radio correlation for sBzKs, and is not indicative of a truly independent estimate of star formation. The model of Condon (1992) does estimate star formation from radio luminosity independent of the IR-Radio correlation; $\text{SFR}_{1.4GHz}^{Condon}$ exceeds SFR_{IR+UV} by a factor of 2-4 over the observed redshift range, but the ratio of these two calibrations appears relatively insensitive to redshift.

X-ray SFR indicators show wide variation in their ratios to SFR_{IR+UV} . As discussed in Section 5.4, the calibration of Persic et al. (2004) reflects an independent estimate of star formation compared to IR luminosity. In the lowest redshift bin, $\text{SFR}_{2-10keV}^{Persic}$ has especially large error, see Table 7, which mitigates the discrepancy, evident in Figure 7, with SFR_{IR+UV} at this redshift. In the middle redshift bins, $\text{SFR}_{2-10keV}^{Persic}$ agrees with SFR_{IR+UV} and shows the same trend with redshift as $\text{SFR}_{1.4GHz}^{Bell}$ and SFR_{UV}^{Corr} . In the highest redshift bin, $\text{SFR}_{2-10keV}^{Persic}$ exceeds SFR_{IR+UV} by a factor of four, possibly indicating contamination by obscured AGN at this redshift. $\text{SFR}_{2-10keV}^{Ranalli}$, derived from lower luminosity galaxies in the local universe, tends to underestimate SFR compared to SFR_{IR+UV} except in the lowest redshift bin; the agreement between $\text{SFR}_{2-10keV}^{Ranalli}$ and SFR_{IR+UV} in the highest redshift may be misleading given the possibility of obscured AGN contamination in this bin.

5.6. sBzK Contribution to Star Formation Rate Density

Ascertaining the cosmic star formation rate density, SFRD, at all redshifts will pose important constraints on galaxy evolution theory. However, current photometric selection methods are invariably incomplete, and therefore cosmic SFRD cannot be measured by studying sBzK galaxies alone. Nevertheless, in order to compare our results with the literature, and to determine the contribution of this color selected sample to the total SFRD, we have determined the SFRD for sBzKs in each redshift bin, using the volume densities of our sample indicated in Table 1 and the star formation rates indicated in Table 7. Multiplying the values of SFR_{IR+UV} indicated in Table 7 by the corresponding comoving volume densities indicated in Table 1, we obtain values of the sBzK contribution to the SFRD of $8 \pm 2 \times 10^{-4}$, 0.010 ± 0.001 , 0.014 ± 0.002 , $0.005 \pm 0.001 \text{ M}_{\odot} \text{ yr}^{-1} \text{ Mpc}^{-3}$ for the redshift bins $0.9 < z \leq 1.2$, $1.2 < z \leq 1.5$, $1.5 < z \leq 2.0$, $2.0 < z \leq 3.2$ respectively. These values are illustrated in Figure 8. Previously reported SFRDs for sBzKs include $0.018 \pm 0.004 \text{ M}_{\odot} \text{ yr}^{-1} \text{ Mpc}^{-3}$ in a $K_{sAB} < 22$ survey with SFR determined from X-ray observations (Reddy et al. 2010). These results are consistent, and a likely correction may bring them into even better agreement: The B band images used to identify BzK galaxies in Reddy et al. (2010) were taken with the Subaru telescope, which as pointed out by Kong et al. (2006) has a significantly redder B band filter than the corresponding filter at VLT used by Daddi et al. (2004) in defining the BzK criterion. As discussed in Section 2, not accounting for this correction can produce a significant excess of “sBzK” galaxies that are in fact low redshift contaminants, thus inflating the number densities of sBzK galaxies in Reddy et al. (2010) and tending to overestimate SFRD.

Yoshikawa et al. (2010) measured the sBzK contribution to the SFRD to be 0.089-0.136 $\text{M}_{\odot} \text{ yr}^{-1} \text{ Mpc}^{-3}$ (depending upon assumptions for dust extinction) averaged over the range $1.4 \lesssim z \lesssim 2.6$ in a $K_{AB} < 22.5$ survey with SFRs determined from $\text{H}\alpha$ spectroscopy. We

attempt to correct for the shallower K band imaging depth of the present survey, which has a $K_{Vega} < 20$ ($K_{AB} < 21.8$) below, in order to make a comparison with this deeper survey. However, the sBzK galaxies reported in Yoshikawa et al. (2010) and Lane et al. (2007) are taken from uncorrected (or at least not reported corrected) Subaru B band images and therefore may overestimate the number density of sBzKs and hence their contribution to SFRD.

The number density of sBzKs increases sharply with magnitude; therefore the ~ 1 magnitude difference between the present survey and deeper surveys is significant. We estimate the number of sBzKs that are missed in the present survey and their contribution to the SFRD. Lane et al. (2007) report sBzK number counts to a depth of $K_{AB} = 22.5$, which includes a number density of 8900 deg^{-2} in their deepest magnitude bin. Based on this number density, with the caveats mentioned above about possible contamination by low redshift interlopers, and assuming the same fraction of AGN and poor redshift estimates of the present survey (18%), this deeper imaging predicts 1800 additional sources in the ECDF-S that are not detected in the shallower MUSYC K -band image. Assuming these additional sources have the same redshift distribution as the detected sample, then these undetected sBzKs would contribute an additional volume density of $2.9 \times 10^{-4} \text{ Mpc}^{-3}$, $7.3 \times 10^{-4} \text{ Mpc}^{-3}$, $5.6 \times 10^{-4} \text{ Mpc}^{-3}$, $1.4 \times 10^{-4} \text{ Mpc}^{-3}$ respectively to the redshift binned volume densities indicated in Table 1. The corresponding increased SFRDs for each redshift bin are computed, using the SFR_{IR+UV} estimates in Table 7. They are indicated as red triangles in Figure 8; these corrected sBzK contributions to SFRD are consistent with the results of Yoshikawa et al. (2010). This figure also illustrates the cosmic star formation history from other investigations, as compiled in Hopkins (2007).

Figure 8 illustrates that the contribution of sBzKs to the total cosmic star formation peaks in the redshift range $1.5 < z \leq 2.0$. In this redshift range, averaged sBzKs contribute

$\sim 20\%$ to the total cosmic star formation rate density. However, sBzKs are the broadest color classification of high redshift, star forming galaxies; e.g. they encompass as much as 80% of BM/BX/LBG galaxies when these latter sources are detected to a comparable K band limit (Reddy et al. 2005). Together, these findings may suggest that the distribution of star formation rates in these galaxies is skewed such that relatively rare, high star formation rate systems contribute disproportionately to the total cosmic SFRD, as is found with submillimeter galaxies (Blain et al. 2002). However the combination of a flux-limited survey with color selection efficiencies being a function of redshift makes it very difficult to infer evolution from these average SFRs.

6. Conclusion

The main results of this paper are summarized in Table 7 and Figure 7. For sBzKs in the redshift range $0.9 < z \leq 3.2$, we find agreement to within a factor of two between total star formation rate, $\text{SFR}_{IR+UV} \equiv \text{SFR}_{IR} + \text{SFR}_{UV}$, and UV SFR, corrected for dust with the method of Meurer et al. (1999). Independent L_{IR} estimates demonstrated sBzKs to follow the Meurer et al. (1999) relation of L_{IR}/L_{UV} vs. β for star burst galaxies as opposed to the corresponding relation for normal star forming galaxies in the local universe or AGN.

Similarly, radio SFRs estimated from the calibration of Bell (2003) are in agreement with total SFRs to within a factor of two. The calibration of Bell (2003) is an indirect estimate of IR luminosity using the far IR-radio correlation, as opposed to an independent calibration based on radio luminosity alone. The SFR calibration of Condon (1992) uses an independent model of radio emission and is consistent with total SFR to within factors of 2-4 over this redshift range.

The X-ray calibration of Persic et al. (2004) uses an independent model of X-ray

emission from HMXBs as a proxy for star formation, and we find the resulting SFR to be discrepant with total SFR by at most a factor of 4, and possibly substantially less, given that X-ray emission in our highest redshift bin may be contaminated by heavily obscured AGN. The X-ray calibration of Ranalli et al. (2003) underestimates the total SFR at high redshift by factors of 3-5 although better agreement is found in the lowest redshift bin (AGN contamination may be responsible for the nominal agreement in the highest redshift bin).

The factor of two discrepancies between the radio SFR calibrations of Bell (2003) and Condon (1992) are not entirely surprising given the different assumptions of each calibration. Discrepancies between X-ray calibrations determined from Persic et al. (2004) and Ranalli et al. (2003) are understood by considering the different methods of each calibration and the galaxy samples underlying them; the Persic et al. (2004) calibration may be more suited to high luminosity, high redshift galaxies, although it requires an assumption of the HMXB luminosity fraction.

In the highest redshift bin, $2.0 < z \leq 3.2$, IR luminosities and SFR estimates from 24 μm only data exceed IR luminosity from panchromatic SED fitting and resulting total SFR by a factor of ≈ 6 . Fitting panchromatic SEDs to spectral templates yields a more robust estimate of the IR luminosity than single band estimates. In particular, the 24 μm band only estimate should be avoided for galaxies at $z \gtrsim 2$.

Our analysis of sBzKs in the redshift range $0.9 < z \leq 3.2$ confirms that they are IR luminous, star forming galaxies for which approximately 90% of the total star formation is obscured by dust. X-ray stacking suggests that when individually detected sources are removed, the remaining sBzK sample is free from obscured AGN contamination, except possibly in the highest redshift bin. By fitting the redshift bin averaged spectra in the range $1.2 < z \leq 1.5$ and $1.5 < z \leq 2.0$ to gray body templates, we find average dust temperatures

of 41 K and 43 K respectively, consistent with star formation induced heating. By fitting to Chary & Elbaz (2001) templates, we find average IR luminosities for redshift binned sBzK galaxies at median redshifts 1.1, 1.4, 1.8, 2.2 to be $0.6 \pm 0.2 \times 10^{11} L_{\odot}$, $3.2 \pm 0.4 \times 10^{11} L_{\odot}$, $5.5 \pm 0.8 \times 10^{11} L_{\odot}$, $6.9 \pm 1.6 \times 10^{11} L_{\odot}$, consistent with the luminosities of LIRGs in the local universe. We find SFR_{IR+UV} at these redshifts to be 12 ± 3 , 58 ± 7 , 100 ± 14 , $130 \pm 28 M_{\odot} \text{ yr}^{-1}$ respectively, and we obtain values of the sBzK contribution to the SFRD to be $8 \pm 2 \times 10^{-4}$, 0.010 ± 0.001 , 0.014 ± 0.002 , $0.005 \pm 0.001 M_{\odot} \text{ yr}^{-1} \text{ Mpc}^{-3}$. These reported contributions to the SFRD are affected by the relatively shallow K band imaging depth of our data, compared to other surveys. Based on extrapolating the galaxy number counts to the faintest reported imaging depth for sBzKs, we estimate their contribution to the cosmic SFRD to be $\sim 20\%$ in the redshift range $1.5 < z \leq 2.0$ where sBzK selection is most efficient.

Support for this work was provided by the National Science Foundation under grant AST-0807570, and by NASA through an award issued by JPL/Caltech. EG thanks U.C. Davis for hospitality during the preparation of this manuscript. Support for the work of ET was provided by the National Aeronautics and Space Administration through Chandra Postdoctoral Fellowship Award Number PF8-90055 issued by the Chandra X-ray Observatory Center, which is operated by the Smithsonian Astrophysical Observatory for an on behalf of the National Aeronautics and Space Administration under contract NAS8-03060. We acknowledge valuable conversations and comments by Viviana Acquaviva, Nicholas A. Bond, Lucia Guaita, Felipe Menanteau, and Axel Weiss and we thank LESS for providing the residual map, obtained from LABOCA APEX RUN IDs: 078.F-9028(A), 079.F-9500(A), 080.A-3023(A), and 081.F-9500(A)

7. Appendix: Error Estimation in Stacking

7.1. Ordinary Average

Section 3 presents the method used in this paper for estimating the aggregate flux, μ , from N prior positions that include a combination of I individual detections, \mathbf{x}_i , and a stacking detection, \mathbf{x}_S , from S undetected sources, where $N = I + S$, given by

$$\mu = \frac{1}{N} \left(\sum_{i=1}^I x_i + S x_s \right) \quad (15)$$

The variance σ_μ^2 of this estimate is related to the individual errors σ_i and σ_s as well as their covariances, $\sigma_{i,s}$ from standard error analysis

$$\sigma_\mu^2 = \sum_{i=1}^I \left(\frac{\partial \mu}{\partial x_i} \right)^2 \sigma_{x_i}^2 + \left(\frac{\partial \mu}{\partial x_s} \right)^2 \sigma_{x_s}^2 + \sum_{i=1}^I 2\sigma_{i,s}^2 \frac{\partial \mu}{\partial x_i} \frac{\partial \mu}{\partial x_s} + \dots \quad (16)$$

We assume that the covariances $\sigma_{i,s}$ are zero.

$$\sigma_\mu^2 = \sum_{i=1}^I \left(\frac{\partial \mu}{\partial x_i} \right)^2 \sigma_{x_i}^2 + \left(\frac{\partial \mu}{\partial x_s} \right)^2 \sigma_{x_s}^2 \quad (17)$$

$$\sigma_\mu^2 = \frac{1}{N^2} \sum_{i=1}^I \sigma_{x_i}^2 + \left(\frac{S}{N} \right)^2 \sigma_{x_s}^2 \quad (18)$$

$$\sigma_\mu = \frac{1}{N} \sqrt{\sum_{i=1}^I \sigma_{x_i}^2 + S^2 \sigma_{x_s}^2} \quad (19)$$

Equations 15 and 19 are used to compute the average and error, respectively, of individual and stacking detections reported in this paper.

In the case of all measurement errors being equal, which is a good approximation in the case of LESS data, then $\sigma_i \equiv \sigma$ and $\sigma_s = \sigma/\sqrt{N}$. Using Equation 19, σ_μ is computed as

$$\sigma_\mu = \frac{1}{N} \sqrt{\sum_{i=1}^I \sigma^2 + S^2 \frac{\sigma^2}{S}} \quad (20)$$

$$\sigma_\mu = \frac{1}{I+S} \sqrt{I\sigma^2 + S\sigma^2} \quad (21)$$

$$\sigma_\mu = \frac{1}{\sqrt{I+S}} \sigma \quad (22)$$

7.2. Weighted average:

An alternative approach to combining individual and stacking detections into a single aggregate flux estimate is to use a weighted average of individual and stacking detections. Assume there are $N = I + 1$ flux measurements consisting of I individual detections and a single stacking detection. Each individual flux measurement and the stacked flux measurement is considered as an independent flux measurement for the purpose of computing an average, and these measurements are combined as an inverse variance weighted average.

$$\mu' = \frac{\sum_{i=1}^N \frac{x_i}{\sigma_i^2}}{\sum_{i=1}^N \frac{1}{\sigma_i^2}} \quad (23)$$

$$\sigma_{\mu'}^2 = \frac{1}{\sum \frac{1}{\sigma_i^2}} \quad (24)$$

Equations 23 and 24 are also used to estimate the aggregate flux and error for representative data reported in this paper. In particular, the errors computed according to this method are numerically equal to the errors computed from the ordinary average, Equation 19, to better than three significant digits.

For clarity, Equation 24 can be written to include stacking and individual detections separately

$$\sigma_{\mu'}^2 = \frac{1}{\sum_{i=1}^I \frac{1}{\sigma_i^2} + \frac{1}{\sigma_s^2}} \quad (25)$$

In the case of all measurement errors being equal, Equation 25 can be simplified using $\sigma_i \equiv \sigma$ and $\sigma_s = \sigma/\sqrt{N}$, just as in the ordinary average error computation:

$$\sigma_{\mu'}^2 = \frac{1}{\sum_{i=1}^I \frac{1}{\sigma^2} + \frac{S}{\sigma^2}} \quad (26)$$

$$\sigma_{\mu'}^2 = \frac{\sigma^2}{I + S} \quad (27)$$

$$\sigma_{\mu'} = \frac{\sigma}{\sqrt{I + S}} \quad (28)$$

Thus for the case of all measurement errors being equal, the error of the weighted average is identical to the error of the ordinary average.

7.3. Comparison of ordinary and weighted average:

In the case of identical errors for the individual measurements, $\sigma_i \equiv \sigma$, then weighted and ordinary averages give the same result for the aggregate flux. In the case of measurement errors being unequal, then the weighted average will in principle have the smaller error; however, the difference will be small, and if the errors are not independent, e.g. if brighter sources have larger errors, then the weighted average introduces a bias to the flux estimate μ' . For instance, if dim sources are always measured with better precision than bright sources, then a weighted average of the population of all sources will always be biased toward dim sources. This circumstance could arise if flux measurement errors are dominated by Poisson counting statistics. However, if the flux measurement errors are uncorrelated with the flux, then there will be no problem with the weighted average.

REFERENCES

- Adelberger, K. L. & Steidel, C. C. 2000, *ApJ*, 544, 218
- Bauer, F. E., Alexander, D. M., Brandt, W. N., Hornschemeier, A. E., Vignali, C., Garmire, G. P., & Schneider, D. P. 2002, *AJ*, 124, 2351
- Bell, E. F. 2003, *ApJ*, 586, 794
- Blain, A. W., Smail, I., Ivison, R. J., Kneib, J., & Frayer, D. T. 2002, *Phys. Rep.*, 369, 111
- Blanc, G. A., Lira, P., Barrientos, L. F., Aguirre, P., Francke, H., Taylor, E. N., Quadri, R., Marchesini, D., Infante, L., Gawiser, E., Hall, P. B., Willis, J. P., Herrera, D., & Maza, J. 2008, *ApJ*, 681, 1099
- Boissier, S., Gil de Paz, A., Boselli, A., Madore, B. F., Buat, V., Cortese, L., Burgarella, D., Muñoz-Mateos, J. C., Barlow, T. A., Forster, K., Friedman, P. G., Martin, D. C., Morrissey, P., Neff, S. G., Schiminovich, D., Seibert, M., Small, T., Wyder, T. K., Bianchi, L., Donas, J., Heckman, T. M., Lee, Y., Milliard, B., Rich, R. M., Szalay, A. S., Welsh, B. Y., & Yi, S. K. 2007, *ApJS*, 173, 524
- Brammer, G. B., van Dokkum, P. G., & Coppi, P. 2008, *ApJ*, 686, 1503
- Buat, V., Giovannoli, E., Burgarella, D., Altieri, B., Amblard, A., Arumugam, V., Aussel, H., Babbedge, T., Blain, A., Bock, J., Boselli, A., Castro-Rodriguez, N., Cava, A., Chanial, P., Clements, D. L., Conley, A., Conversi, L., Cooray, A., Dowell, C. D., Dwek, E., Eales, S., Elbaz, D., Fox, M., Franceschini, A., Gear, W., Glenn, J., Griffin, M., Halpern, M., Hatziminaoglou, E., Heinis, S., Ibar, E., Isaak, K., Ivison, R. J., Lagache, G., Levenson, L., Lonsdale, C. J., Lu, N., Madden, S., Maffei, B., Magdis, G., Mainetti, G., Marchetti, L., Morrison, G. E., Nguyen, H. T., O’Halloran, B., Oliver, S. J., Omont, A., Owen, F. N., Page, M. J., Pannella, M., Panuzzo, P.,

- Papageorgiou, A., Pearson, C. P., Perez-Fournon, I., Pohlen, M., Rigopoulou, D., Rizzo, D., Roseboom, I. G., Rowan-Robinson, M., Sanchez Portal, M., Schulz, B., Seymour, N., Shupe, D. L., Smith, A. J., Stevens, J. A., Strazzullo, V., Symeonidis, M., Trichas, M., Tugwell, K. E., Vaccari, M., Valiante, E., Valtchanov, I., Vigroux, L., Wang, L., Ward, R., Wright, G., Xu, C. K., & Zemcov, M. 2010, ArXiv e-prints
- Buat, V., Takeuchi, T. T., Iglesias-Páramo, J., Xu, C. K., Burgarella, D., Boselli, A., Barlow, T., Bianchi, L., Donas, J., Forster, K., Friedman, P. G., Heckman, T. M., Lee, Y., Madore, B. F., Martin, D. C., Milliard, B., Morissey, P., Neff, S., Rich, M., Schiminovich, D., Seibert, M., Small, T., Szalay, A. S., Welsh, B., Wyder, T., & Yi, S. K. 2007, *ApJS*, 173, 404
- Calzetti, D. 2008, in *Astronomical Society of the Pacific Conference Series*, Vol. 390, *Pathways Through an Eclectic Universe*, ed. J. H. Knapen, T. J. Mahoney, & A. Vazdekis, 121–+
- Calzetti, D., Kinney, A. L., & Storchi-Bergmann, T. 1994, *ApJ*, 429, 582
- Cardamone, C. N., van Dokkum, P. G., Urry, C. M., Taniguchi, Y., Gawiser, E., Brammer, G., Taylor, E., Damen, M., Treister, E., Cobb, B. E., Bond, N., Schawinski, K., Lira, P., Murayama, T., Saito, T., & Sumikawa, K. 2010, *ApJS*, 189, 270
- Chary, R. & Elbaz, D. 2001, *ApJ*, 556, 562
- Condon, J. J. 1974, *ApJ*, 188, 279
- . 1992, *ARA&A*, 30, 575
- Daddi, E., Alexander, D. M., Dickinson, M., Gilli, R., Renzini, A., Elbaz, D., Cimatti, A., Chary, R., Frayer, D., Bauer, F. E., Brandt, W. N., Giavalisco, M., Grogin, N. A.,

- Huynh, M., Kurk, J., Mignoli, M., Morrison, G., Pope, A., & Ravindranath, S. 2007a, *ApJ*, 670, 173
- Daddi, E., Cimatti, A., Renzini, A., Fontana, A., Mignoli, M., Pozzetti, L., Tozzi, P., & Zamorani, G. 2004, *ApJ*, 617, 746
- Daddi, E., Dickinson, M., Chary, R., Pope, A., Morrison, G., Alexander, D. M., Bauer, F. E., Brandt, W. N., Giavalisco, M., Ferguson, H., Lee, K.-S., Lehmer, B. D., Papovich, C., & Renzini, A. 2005, *ApJ*, 631, L13
- Daddi, E., Dickinson, M., Morrison, G., Chary, R., Cimatti, A., Elbaz, D., Frayer, D., Renzini, A., Pope, A., Alexander, D. M., Bauer, F. E., Giavalisco, M., Huynh, M., Kurk, J., & Mignoli, M. 2007b, *ApJ*, 670, 156
- Dale, D. A. & Helou, G. 2002, *ApJ*, 576, 159
- Dannerbauer, H., Daddi, E., Onodera, M., Kong, X., Röttgering, H., Arimoto, N., Brusa, M., Cimatti, A., Kurk, J., Lehnert, M. D., Mignoli, M., & Renzini, A. 2006, *ApJ*, 637, L5
- Devlin, M. J., Ade, P. A. R., Aretxaga, I., Bock, J. J., Chapin, E. L., Griffin, M., Gundersen, J. O., Halpern, M., Hargrave, P. C., Hughes, D. H., Klein, J., Marsden, G., Martin, P. G., Mauskopf, P., Moncelsi, L., Netterfield, C. B., Ngo, H., Olmi, L., Pascale, E., Patanchon, G., Rex, M., Scott, D., Semisch, C., Thomas, N., Truch, M. D. P., Tucker, C., Tucker, G. S., Viero, M. P., & Wiebe, D. V. 2009, *Nature*, 458, 737
- Dunne, L., Ivison, R. J., Maddox, S., Cirasuolo, M., Mortier, A. M., Foucaud, S., Ibar, E., Almaini, O., Simpson, C., & McLure, R. 2009, *MNRAS*, 394, 3
- Garn, T., Sobral, D., Best, P. N., Geach, J. E., Smail, I., Cirasuolo, M., Dalton, G. B., Dunlop, J. S., McLure, R. J., & Farrah, D. 2010, *MNRAS*, 402, 2017

- Gawiser, E., van Dokkum, P. G., Herrera, D., Maza, J., Castander, F. J., Infante, L., Lira, P., Quadri, R., Toner, R., Treister, E., Urry, C. M., Altmann, M., Assef, R., Christlein, D., Coppi, P. S., Durán, M. F., Franx, M., Galaz, G., Huerta, L., Liu, C., López, S., Méndez, R., Moore, D. C., Rubio, M., Ruiz, M. T., Toft, S., & Yi, S. K. 2006, *ApJS*, 162, 1
- Genzel, R., Tacconi, L. J., Eisenhauer, F., Förster Schreiber, N. M., Cimatti, A., Daddi, E., Bouché, N., Davies, R., Lehnert, M. D., Lutz, D., Nesvadba, N., Verma, A., Abuter, R., Shapiro, K., Sternberg, A., Renzini, A., Kong, X., Arimoto, N., & Mignoli, M. 2006, *Nature*, 442, 786
- Gilfanov, M., Grimm, H., & Sunyaev, R. 2004, *MNRAS*, 347, L57
- Greve, T. R., Weiß, A., Walter, F., Smail, I., Zheng, X. Z., Knudsen, K. K., Coppin, K. E. K., Kovács, A., Bell, E. F., de Breuck, C., Dannerbauer, H., Dickinson, M., Gawiser, E., Lutz, D., Rix, H., Schinnerer, E., Alexander, D., Bertoldi, F., Brandt, N., Chapman, S. C., Ivison, R. J., Koekemoer, A. M., Kreysa, E., Kurczynski, P., Menten, K., Siringo, G., Swinbank, M., & van der Werf, P. 2010, *ApJ*, 719, 483
- Grimm, H., Gilfanov, M., & Sunyaev, R. 2003, *MNRAS*, 339, 793
- Haarsma, D. B., Partridge, R. B., Windhorst, R. A., & Richards, E. A. 2000, *ApJ*, 544, 641
- Hayashi, M., Shimasaku, K., Motohara, K., Yoshida, M., Okamura, S., & Kashikawa, N. 2007, *ApJ*, 660, 72
- Helou, G., Khan, I. R., Malek, L., & Boehmer, L. 1988, *ApJS*, 68, 151
- Hogg, D. W. 2001, *AJ*, 121, 1207
- Hopkins, A. M. 2007, in *Astronomical Society of the Pacific Conference Series*, Vol. 380,

- Deepest Astronomical Surveys, ed. J. Afonso, H. C. Ferguson, B. Mobasher, & R. Norris, 423–+
- Howell, J. H., Armus, L., Mazzarella, J. M., Evans, A. S., Surace, J. A., Sanders, D. B., Petric, A., Appleton, P., Bothun, G., Bridge, C., Chan, B. H. P., Charmandaris, V., Frayer, D. T., Haan, S., Inami, H., Kim, D., Lord, S., Madore, B. F., Melbourne, J., Schulz, B., U, V., Vavilkin, T., Veilleux, S., & Xu, K. 2010, *ApJ*, 715, 572
- Huynh, M. T., Pope, A., Frayer, D. T., & Scott, D. 2007, *ApJ*, 659, 305
- Iverson, R. J., Alexander, D. M., Biggs, A. D., Brandt, W. N., Chapin, E. L., Coppin, K. E. K., Devlin, M. J., Dickinson, M., Dunlop, J., Dye, S., Eales, S. A., Frayer, D. T., Halpern, M., Hughes, D. H., Ibar, E., Kovács, A., Marsden, G., Monceli, L., Netterfield, C. B., Pascale, E., Patanchon, G., Rafferty, D. A., Rex, M., Schinnerer, E., Scott, D., Semisch, C., Smail, I., Swinbank, A. M., Truch, M. D. P., Tucker, G. S., Viero, M. P., Walter, F., Weiß, A., Wiebe, D. V., & Xue, Y. Q. 2010a, *MNRAS*, 402, 245
- Iverson, R. J., Chapman, S. C., Faber, S. M., Smail, I., Biggs, A. D., Conselice, C. J., Wilson, G., Salim, S., Huang, J.-S., & Willner, S. P. 2007, *ApJ*, 660, L77
- Iverson, R. J., Magnelli, B., Ibar, E., Andreani, P., Elbaz, D., Altieri, B., Amblard, A., Arumugam, V., Auld, R., Aussel, H., Babbedge, T., Berta, S., Blain, A., Bock, J., Bongiovanni, A., Boselli, A., Buat, V., Burgarella, D., Castro-Rodríguez, N., Cava, A., Cepa, J., Chanical, P., Cimatti, A., Cirasuolo, M., Clements, D. L., Conley, A., Conversi, L., Cooray, A., Daddi, E., Dominguez, H., Dowell, C. D., Dwek, E., Eales, S., Farrah, D., Förster Schreiber, N., Fox, M., Franceschini, A., Gear, W., Genzel, R., Glenn, J., Griffin, M., Gruppioni, C., Halpern, M., Hatziminaoglou, E., Isaak, K., Lagache, G., Levenson, L., Lu, N., Lutz, D., Madden, S., Maffei, B., Magdis,

- G., Mainetti, G., Maiolino, R., Marchetti, L., Morrison, G. E., Mortier, A. M. J., Nguyen, H. T., Nordon, R., O'Halloran, B., Oliver, S. J., Omont, A., Owen, F. N., Page, M. J., Panuzzo, P., Papageorgiou, A., Pearson, C. P., Pérez-Fournon, I., Pérez García, A. M., Poglitsch, A., Pohlen, M., Popesso, P., Pozzi, F., Rawlings, J. I., Raymond, G., Rigopoulou, D., Riguccini, L., Rizzo, D., Rodighiero, G., Roseboom, I. G., Rowan-Robinson, M., Saintonge, A., Sanchez Portal, M., Santini, P., Schulz, B., Scott, D., Seymour, N., Shao, L., Shupe, D. L., Smith, A. J., Stevens, J. A., Sturm, E., Symeonidis, M., Tacconi, L., Trichas, M., Tugwell, K. E., Vaccari, M., Valtchanov, I., Vieira, J., Vigroux, L., Wang, L., Ward, R., Wright, G., Xu, C. K., & Zemcov, M. 2010b, *A&A*, 518, L31+
- Kennicutt, R. C., Hao, C., Calzetti, D., Moustakas, J., Dale, D. A., Bendo, G., Engelbracht, C. W., Johnson, B. D., & Lee, J. C. 2009, *ApJ*, 703, 1672
- Kennicutt, Jr., R. C. 1998, *ARA&A*, 36, 189
- Kong, X., Charlot, S., Brinchmann, J., & Fall, S. M. 2004, *MNRAS*, 349, 769
- Kong, X., Daddi, E., Arimoto, N., Renzini, A., Broadhurst, T., Cimatti, A., Ikuta, C., Ohta, K., da Costa, L., Olsen, L. F., Onodera, M., & Tamura, N. 2006, *ApJ*, 638, 72
- Kroupa, P. 2001, in *Astronomical Society of the Pacific Conference Series*, Vol. 228, *Dynamics of Star Clusters and the Milky Way*, ed. S. Deiters, B. Fuchs, A. Just, R. Spurzem, & R. Wielen, 187–+
- Kurczynski, P. & Gawiser, E. 2010, *AJ*, 139, 1592
- Lagache, G., Dole, H., & Puget, J. 2003, *MNRAS*, 338, 555
- Lane, K. P., Almaini, O., Foucaud, S., Simpson, C., Smail, I., McLure, R. J., Conselice,

- C. J., Cirasuolo, M., Page, M. J., Dunlop, J. S., Hirst, P., Watson, M. G., & Sekiguchi, K. 2007, MNRAS, 379, L25
- Lehmer, B. D., Brandt, W. N., Alexander, D. M., Bauer, F. E., Schneider, D. P., Tozzi, P., Bergeron, J., Garmire, G. P., Giacconi, R., Gilli, R., Hasinger, G., Hornschemeier, A. E., Koekemoer, A. M., Mainieri, V., Miyaji, T., Nonino, M., Rosati, P., Silverman, J. D., Szokoly, G., & Vignali, C. 2005, ApJS, 161, 21
- Lutovinov, A., Revnivtsev, M., Gilfanov, M., Shtykovskiy, P., Molkov, S., & Sunyaev, R. 2005, A&A, 444, 821
- Madau, P. 1995, ApJ, 441, 18
- Marsden, G., Ade, P. A. R., Bock, J. J., Chapin, E. L., Devlin, M. J., Dicker, S. R., Griffin, M., Gundersen, J. O., Halpern, M., Hargrave, P. C., Hughes, D. H., Klein, J., Mauskopf, P., Magnelli, B., Moncelsi, L., Netterfield, C. B., Ngo, H., Olmi, L., Pascale, E., Patanchon, G., Rex, M., Scott, D., Semisch, C., Thomas, N., Truch, M. D. P., Tucker, C., Tucker, G. S., Viero, M. P., & Wiebe, D. V. 2009, ApJ, 707, 1729
- McCracken, H. J., Capak, P., Salvato, M., Aussel, H., Thompson, D., Daddi, E., Sanders, D. B., Kneib, J., Willott, C. J., Mancini, C., Renzini, A., Cook, R., Le Fèvre, O., Ilbert, O., Kartaltepe, J., Koekemoer, A. M., Mellier, Y., Murayama, T., Scoville, N. Z., Shioya, Y., & Tanaguchi, Y. 2010, ApJ, 708, 202
- Meurer, G. R., Heckman, T. M., & Calzetti, D. 1999, ApJ, 521, 64
- Miller, N. A., Fomalont, E. B., Kellermann, K. I., Mainieri, V., Norman, C., Padovani, P., Rosati, P., & Tozzi, P. 2008, ApJS, 179, 114

- Murphy, E. J., Chary, R., Alexander, D. M., Dickinson, M., Magnelli, B., Morrison, G., Pope, A., & Teplitz, H. I. 2009, *ApJ*, 698, 1380
- Muzzin, A., van Dokkum, P., Kriek, M., Labbe, I., Cury, I., Marchesini, D., & Franx, M. 2010, *ArXiv e-prints*
- Pannella, M., Carilli, C. L., Daddi, E., McCracken, H. J., Owen, F. N., Renzini, A., Strazzullo, V., Civano, F., Koekemoer, A. M., Schinnerer, E., Scoville, N., Smolčić, V., Taniguchi, Y., Aussel, H., Kneib, J. P., Ilbert, O., Mellier, Y., Salvato, M., Thompson, D., & Willott, C. J. 2009, *ApJ*, 698, L116
- Papovich, C., Rudnick, G., Le Floch, E., van Dokkum, P. G., Rieke, G. H., Taylor, E. N., Armus, L., Gawiser, E., Huang, J., Marcillac, D., & Franx, M. 2007, *ApJ*, 668, 45
- Peeters, E., Spoon, H. W. W., & Tielens, A. G. G. M. 2004, *ApJ*, 613, 986
- Persic, M. & Rephaeli, Y. 2002, *A&A*, 382, 843
- Persic, M., Rephaeli, Y., Braito, V., Cappi, M., Della Ceca, R., Franceschini, A., & Gruber, D. E. 2004, *A&A*, 419, 849
- Ranalli, P., Comastri, A., & Setti, G. 2003, *A&A*, 399, 39
- Reddy, N. A., Erb, D. K., Pettini, M., Steidel, C. C., & Shapley, A. E. 2010, *ApJ*, 712, 1070
- Reddy, N. A., Erb, D. K., Steidel, C. C., Shapley, A. E., Adelberger, K. L., & Pettini, M. 2005, *ApJ*, 633, 748
- Reddy, N. A., Steidel, C. C., Fadda, D., Yan, L., Pettini, M., Shapley, A. E., Erb, D. K., & Adelberger, K. L. 2006, *ApJ*, 644, 792
- Salpeter, E. E. 1955, *ApJ*, 121, 161

- Siebenmorgen, R. & Krügel, E. 2007, *A&A*, 461, 445
- Silva, L., Granato, G. L., Bressan, A., & Danese, L. 1998, *ApJ*, 509, 103
- Symeonidis, M., Willner, S. P., Rigopoulou, D., Huang, J., Fazio, G. G., & Jarvis, M. J. 2008, *MNRAS*, 385, 1015
- Takagi, T., Ono, Y., Shimasaku, K., & Hanami, H. 2008, *MNRAS*, 389, 775
- Takeuchi, T. T., Buat, V., & Burgarella, D. 2005, *A&A*, 440, L17
- Takeuchi, T. T., Buat, V., Heinis, S., Giovannoli, E., Yuan, F., Iglesias-Páramo, J., Murata, K. L., & Burgarella, D. 2010, *A&A*, 514, A4+
- Taylor, E. N., Franx, M., van Dokkum, P. G., Quadri, R. F., Gawiser, E., Bell, E. F., Barrientos, L. F., Blanc, G. A., Castander, F. J., Damen, M., Gonzalez-Perez, V., Hall, P. B., Herrera, D., Hildebrandt, H., Kriek, M., Labbé, I., Lira, P., Maza, J., Rudnick, G., Treister, E., Urry, C. M., Willis, J. P., & Wuyts, S. 2009, *ApJS*, 183, 295
- Tielens, A. G. G. M. 2008, *ARA&A*, 46, 289
- Truch, M. D. P., Ade, P. A. R., Bock, J. J., Chapin, E. L., Devlin, M. J., Dicker, S., Griffin, M., Gundersen, J. O., Halpern, M., Hargrave, P. C., Hughes, D. H., Klein, J., Marsden, G., Martin, P. G., Mauskopf, P., Netterfield, C. B., Olmi, L., Pascale, E., Patanchon, G., Rex, M., Scott, D., Semisch, C., Tucker, C., Tucker, G. S., Viero, M. P., & Wiebe, D. V. 2008, *ApJ*, 681, 415
- Virani, S. N., Treister, E., Urry, C. M., & Gawiser, E. 2006, *AJ*, 131, 2373
- Weiss, A., Kovacs, A., Coppin, K., Greve, T. R., Walter, F., Smail, I., Dunlop, J. S., Knudsen, K. K., Alexander, D. M., Bertoldi, F., Brandt, W. N., Chapman, S. C.,

- Cox, P., Dannerbauer, H., De Breuck, C., Gawiser, E., Ivison, R. J., Lutz, D.,
Menten, K. M., Koekemoer, A. M., Kreysa, E., Kurczynski, P., Rix, H., Schinnerer,
E., & van der Werf, P. P. 2009, *ApJ*, 707
- Yoshikawa, T., Akiyama, M., Kajisawa, M., Alexander, D. M., Ohta, K., Suzuki, R.,
Tokoku, C., Uchimoto, Y. K., Konishi, M., Yamada, T., Tanaka, I., Omata, K.,
Nishimura, T., Koekemoer, A. M., Brandt, N., & Ichikawa, T. 2010, *ApJ*, 718, 112
- Yun, M. S., Reddy, N. A., & Condon, J. J. 2001, *ApJ*, 554, 803

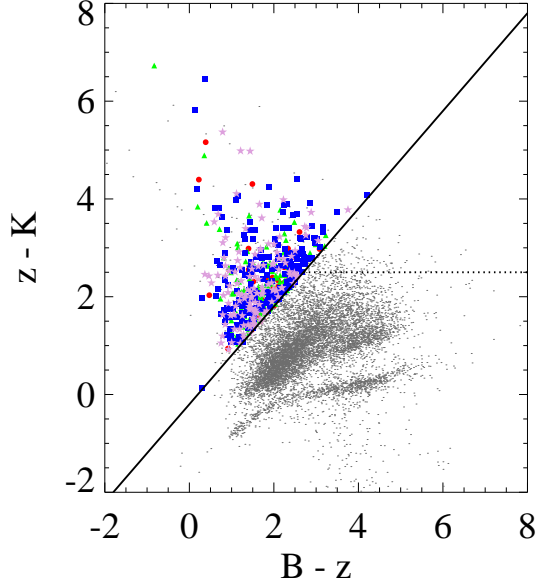


Fig. 1.— BzK diagram illustrating corrected NIR-optical colors $(z - K)_{AB}$ vs. $(B - z)_{AB}$ for MUSYC $K < 21.8$ selected sources (gray points), including redshift binned, star forming galaxies (with AGN removed, see text) in the range $0.9 < z \leq 1.2$ (red circles), $1.2 < z \leq 1.5$ (green triangles), $1.5 < z \leq 2.0$ (blue squares) and $2.0 < z \leq 3.2$ (purple stars). The $sBzK$ region is located above the diagonal line, and is defined as $BzK \geq 0.2$. The $pBzK$ region is the wedge shaped area defined by the horizontal dotted line, $z - K = 2.5$.

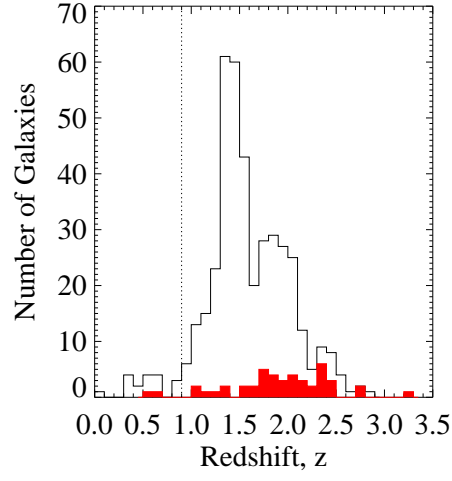


Fig. 2.— Histograms of photometric and spectroscopic redshifts for sBzK galaxies in ECDF-S. Upper curve indicates photometric redshifts. Lower filled (red), histogram indicates spectroscopic redshifts. Vertical dotted line indicates $z < 0.9$ galaxies that are excluded from analysis.

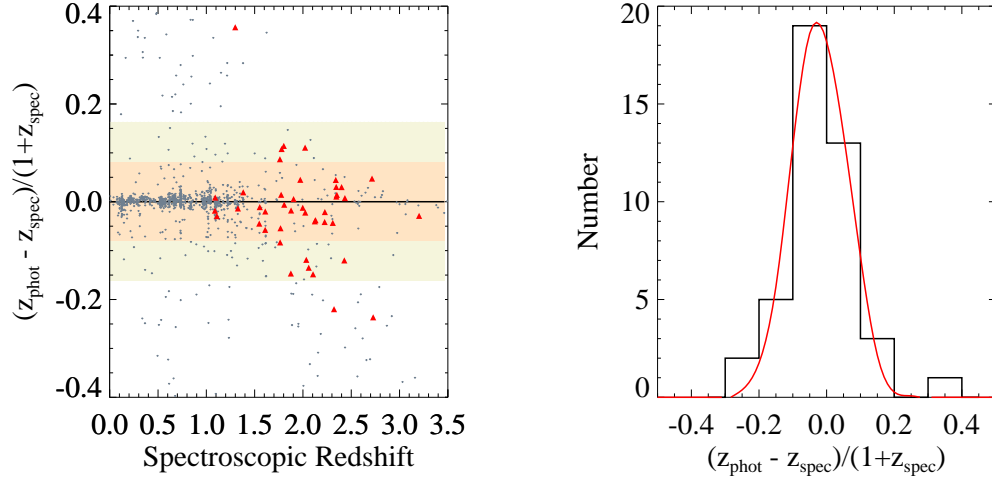


Fig. 3.— Left figure illustrates photometric redshift error, defined as $(z_{\text{phot}} - z_{\text{spec}})/(1 + z_{\text{spec}})$, vs. spectroscopic redshift for K selected galaxies in ECDF-S. Triangles (red) illustrate sBzK galaxies. 1σ and 2σ regions, determined from the histogram (right figure) are indicated by shading. Points (gray) illustrate all 1285 K selected galaxies for which spectroscopic and photometric redshifts are available. Right figure illustrates histogram of photometric redshift errors for sBzK galaxies along with a Gaussian fit (mean = -0.02 and $\sigma = 0.08$).

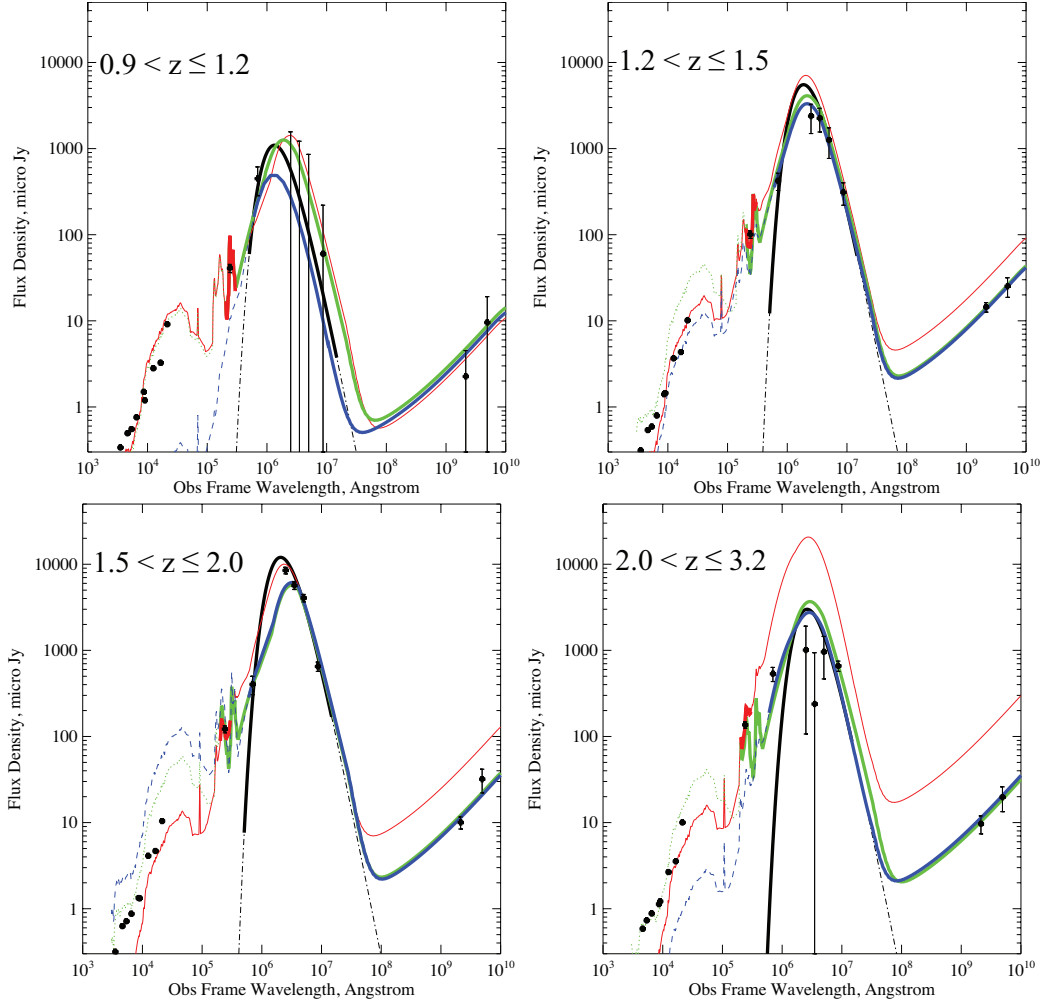


Fig. 4.— Spectral energy distribution fits of redshift binned sBzK galaxies to various models. Spectrum flux density, in units of μJy , is plotted vs. observed frame wavelength, in units of Angstroms. UV through radio flux measurements are indicated by points with error bars. Curves indicate best fit models: dotted (green) CE01 template fitted to the $\lambda \geq 24\mu\text{m}$ spectrum, dashed (blue) CE01 template fitted to the $\lambda > 24\mu\text{m}$ spectrum, dot-dashed (gray) graybody (emissivity index, $\beta=1.5$) fitted to the FIR-submm peak, dot-dot-dash (red) CE01 template fitted to only the $24\mu\text{m}$ data point. For each model fit, the region of the spectrum used for the fit is indicated by the solid portion of the curve. Upper left: galaxies in the redshift range $0.9 < z \leq 1.2$; upper right $1.2 < z \leq 1.5$; lower left $1.5 < z \leq 2.0$; lower right $2.0 < z \leq 3.2$. See also Table 4 for fit details.

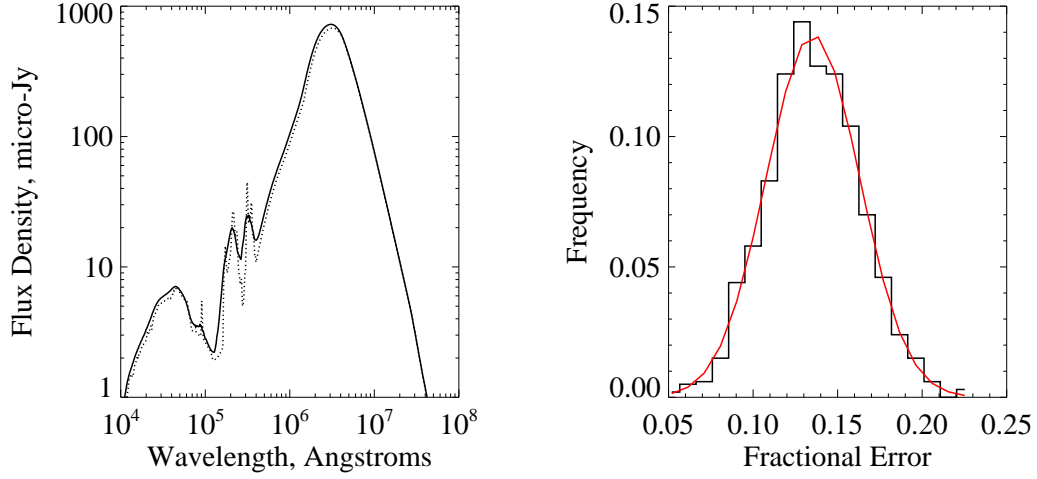


Fig. 5.— Left figure illustrates simulated, observed frame spectra for sBzK galaxies in the range $1.5 < z \leq 2.0$. The dotted curve indicates the best fit CE01 template placed at the median redshift, $z = 1.756$. The solid curve indicates the result of averaging 233 identical CE01 template sources, distributed in redshift according to the observed distribution of sBzKs, with photometric redshift errors added according to the distribution shown in Figure 3. Right figure illustrates the frequency distribution of L_{IR} fractional errors due to photometric redshift errors, for sBzK galaxies in the range $1.5 < z \leq 2.0$. Frequency is determined from the histogram of fractional errors and simulation with 1000 trials. Solid curve (red) indicates a Gaussian fit with mean = 0.14 and $\sigma=0.03$. Thus photometric redshift errors caused L_{IR} for this redshift bin to be overestimated by 14% and contributed a scatter of 3%.

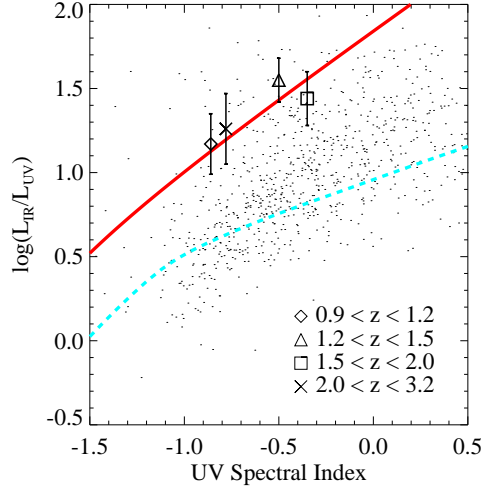


Fig. 6.— $\log(L_{IR}/L_{UV})$ vs UV spectral index, β (where $f_\lambda \propto \lambda^\beta$), for redshift binned sBzK galaxies and IR selected galaxies in the local universe. Symbols with error bars indicate redshift binned sBzK estimates. Points indicate star forming and starburst galaxies in the local universe ($z < 0.3$) taken from Buat et al. (2010). The solid curve (red) indicates the relation for starburst galaxies from Meurer et al. (1999). The dashed curve (cyan) indicates a corresponding relation for normal star forming galaxies in the local universe (Boissier et al. 2007).

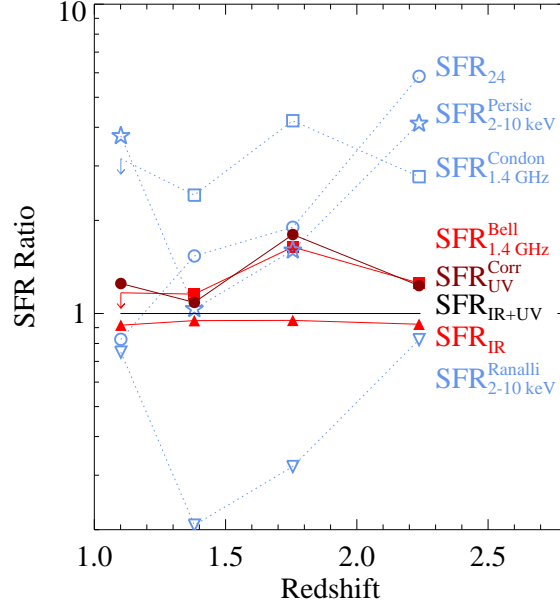


Fig. 7.— Ratio of SFR computed with various calibrations to the bolometric SFR estimate, SFR_{IR+UV} . Filled symbols indicate calibrations that are consistent with SFR_{IR+UV} to within a factor of two in all redshift bins. Upper limits are indicated by arrows. Lines connecting points are a guide to the eye.

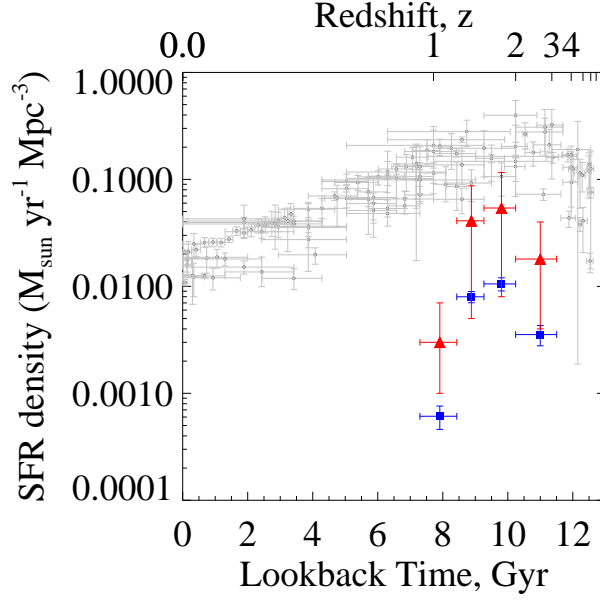


Fig. 8.— sBzK contribution to cosmic star formation history: Star Formation Rate Density (SFRD) vs. lookback time. Blue squares indicate SFRD contributed from redshift binned sBzK galaxies in MUSYC/ECDF-S. Red triangles indicate sBzK contribution to SFRD extrapolated to $K_{AB} < 22.5$ imaging depth, as discussed in the text. Gray points are from the compilation of Hopkins (2007).

Table 1. Redshift binned sample of star forming galaxies (sBzKs) in the ECDF-S

Redshift Range (1)	Median Redshift (2)	Number (z_{phot}, z_{spec}) (3)	Surf. Density, arc min ⁻² (4)	Vol. Density, Mpc ⁻³ (5)
$0.9 < z \leq 1.2$	1.101	49 (46,3)	0.05	6.56×10^{-5}
$1.2 < z \leq 1.5$	1.381	161(157,4)	0.18	1.79×10^{-4}
$1.5 < z \leq 2.0$	1.756	233 (216,17)	0.26	1.37×10^{-4}
$2.0 < z \leq 3.2$	2.237	154 (132,22)	0.17	3.54×10^{-5}

Note. — Redshift binning scheme selected for this analysis. Column (1) indicate the redshift range for each bin. Column (2) indicates the median redshift of the sampled galaxies in each bin, and Column (3) shows the total number of galaxies in each bin, consisting of numbers of galaxies with photometric and spectroscopic redshifts, respectively, in parentheses. Column (4) indicates the density of galaxies on the sky in arc min⁻². Column (5) indicates the corresponding comoving volume density in Mpc⁻³

Table 2. Redshift Binned sBzK X-ray Flux, Luminosity and SFR Estimates

Redshift	Soft Band		Hard Band			
	Flux	Luminosity	Flux	Luminosity	$\text{SFR}_{2-10\text{keV}}^{\text{Ranalli}}$	$\text{SFR}_{2-10\text{keV}}^{\text{Persic}}$
(1)	(2)	(3)	(4)	(5)	(6)	(7)
$0.9 < z \leq 1.2$	<0.87 (1)	0.34	9 ± 8 (1)	4.6	9 ± 8	45 ± 40
$1.2 < z \leq 1.5$	1.5 ± 0.4 (4)	0.94	7 ± 4 (2)	6.0	12 ± 6	60 ± 30
$1.5 < z \leq 2.0$	2.8 ± 0.4 (7)	2.9	11 ± 4 (3)	16	32 ± 11	160 ± 55
$2.0 < z \leq 3.2$	3.8 ± 0.5 (8)	6.5	20 ± 4 (5)	54	107 ± 23	535 ± 115

Note. — Column (1) — the sample bin redshift range. Column (2) — observed flux density in Chandra soft band (0.5-2 keV), in units of $10^{-18} \text{ erg s}^{-1} \text{ cm}^{-2}$. Detection significance (flux/error) is indicated in parenthesis. Column (3) — the luminosity in Chandra soft band (0.5-2 keV), assuming spectrum with photon index, $\Gamma=1.2$ and $E_c=20 \text{ keV}$, at the median redshift. Units are $10^{40} \text{ erg s}^{-1}$. Column (4) — observed flux density in Chandra hard band (2-8 keV), in units of $10^{-18} \text{ erg s}^{-1} \text{ cm}^{-2}$. Detection significance (flux/error) is indicated in parenthesis. Column (5) — the luminosity in Chandra hard band (2-8 keV), assuming spectrum with photon index, $\Gamma=1.2$ and $E_c=20 \text{ keV}$, at the median redshift. Units are $10^{40} \text{ erg s}^{-1}$. Column (6) — SFR from the method of Ranalli et al. (2003) in units of $M_{\odot} \text{ yr}^{-1}$. Column (7) — SFR from the method of Persic et al. (2004).

Table 3. UV-Radio Average Flux Densities for Redshift Binned sBzKs

Band	λ	$0.9 < z \leq 1.2$		$1.2 < z \leq 1.5$		$1.5 < z \leq 2.0$		$2.0 < z \leq 3.2$	
		S_ν	dS_ν	S_ν	dS_ν	S_ν	dS_ν	S_ν	dS_ν
(1)	(2)	(3)	(4)	(5)	(6)	(7)	(8)	(9)	(10)
U	0.35	0.34	0.02	0.31	0.02	0.32	0.02	0.23	0.01
B	0.46	0.49	0.02	0.54	0.03	0.63	0.03	0.58	0.03
V	0.54	0.55	0.03	0.59	0.03	0.72	0.04	0.73	0.04
R	0.65	0.76	0.04	0.79	0.04	0.87	0.04	0.88	0.04
I	0.86	1.50	0.08	1.40	0.07	1.33	0.07	1.13	0.06
z'	0.90	1.19	0.06	1.45	0.07	1.32	0.07	1.22	0.06
J	1.25	2.81	0.15	3.67	0.19	4.11	0.21	2.67	0.14
H	1.65	3.26	0.17	4.34	0.22	4.68	0.24	3.55	0.18
K	2.13	9.13	0.47	10.12	0.51	10.41	0.52	10.03	0.51
24 μm	24.00	40.80	4.50	100.70	10.20	121.60	11.40	136.50	11.90
70 μm	70.00	448.00	165.00	422.00	96.00	403.00	97.00	534.00	100.00
250 μm	250.00	-2684.36	1566.27	2383.17	887.57	8475.42	741.75	1008.16	901.19
350 μm	350.00	-2050.05	1217.80	2250.45	690.33	5661.50	577.76	238.18	701.00

Table 3—Continued

Band	λ	$0.9 < z \leq 1.2$		$1.2 < z \leq 1.5$		$1.5 < z \leq 2.0$		$2.0 < z \leq 3.2$	
		S_ν	dS_ν	S_ν	dS_ν	S_ν	dS_ν	S_ν	dS_ν
(1)	(2)	(3)	(4)	(5)	(6)	(7)	(8)	(9)	(10)
500 μm	500.00	-2711.33	856.83	1254.78	486.30	4057.39	406.51	959.24	493.43
870 μm	870.00	60.00	160.00	310.00	90.00	650.00	80.00	660.00	90.00
1.4 GHz	2.1×10^5	<2.26	0.75	14.44	1.83	10.02	1.60	9.68	2.28
610 MHz	4.9×10^5	<9.55	3.18	25.19	6.45	31.88	9.79	19.70	6.31

Note. — UV-Radio Average flux densities for redshift binned sBzKs. Column (1) — Waveband. Column (2) — Effective, observed frame wavelength in units of μm . Columns (3,5,7,9) — Average, observed flux density in units of μJy for each redshift bin. 1.4 GHz and 610 MHz data in Column (3) indicate 3σ upper limits. Column (4,6,8,10) — Error in flux density in units of μJy for each redshift bin.

Table 4. Redshift Binned sBzK IR-Radio Fit Summary

Redshift	Fit Type	L_{IR}	$\chi^2(\text{df})$	SFR_{IR}
(1)	(2)	(3)	(4)	(5)
$0.9 < z \leq 1.2$	CE01 ($\geq 24 \mu\text{m}$)	0.6 ± 0.2	23.47(7)	11 ± 3
	CE01 ($> 24 \mu\text{m}$)	0.3 ± 0.3	18.96(6)	5 ± 5
	CE01 ($24 \mu\text{m}$)	0.6 ± 0.2	0.17(0)	10 ± 3
	GB (T=50 K)	0.5 ± 0.6	17.74(4)	9 ± 10
$1.2 < z \leq 1.5$	CE01 ($\geq 24 \mu\text{m}$)	3.2 ± 0.4	14.04(7)	55 ± 7
	CE01 ($> 24 \mu\text{m}$)	2.6 ± 0.2	4.64(6)	44 ± 4
	CE01 ($24 \mu\text{m}$)	5.2 ± 0.5	0.01(0)	89 ± 9
	GB	3.3 ± 0.5	3.49(4)	57 ± 8
$1.5 < z \leq 2.0$	CE01 ($\geq 24 \mu\text{m}$)	5.5 ± 0.8	48.40(7)	95 ± 14
	CE01 ($> 24 \mu\text{m}$)	6.1 ± 1.0	43.30(6)	106 ± 18
	CE01 ($24 \mu\text{m}$)	11.3 ± 3.0	0.01(0)	195 ± 51
	GB	11.8 ± 1.8	25.14(4)	203 ± 30
$2.0 < z \leq 3.2$	CE01 ($\geq 24 \mu\text{m}$)	6.9 ± 1.6	44.82(7)	120 ± 28
	CE01 ($> 24 \mu\text{m}$)	5.8 ± 1.5	22.15(6)	100 ± 26
	CE01 ($24 \mu\text{m}$)	44.2 ± 5.0	0.01(0)	761 ± 85
	GB (T=40 K)	4.2 ± 2.5	44.98(4)	72 ± 44

Note. — Column (1) indicates redshift range for the sample. Column (2) specifies the type of model fit (see text). Column (3) indicates the computed L_{IR} from the best fit model, in units of $10^{11} L_{\odot}$. Column (4) indicates the χ^2 value for the best fit, with degrees of freedom in parentheses. Column (5) indicates the SFR, in units of $M_{\odot} \text{ yr}^{-1}$, computed from the fit-derived IR luminosity. Errors correspond to 68% confidence intervals.

Table 5. Redshift Binned sBzK UV Luminosity and SFR Estimates

Redshift	L_{UV}^{Uncorr}	β_{fit}	IRX	A_{1600}	L_{UV}^{Corr}	SFR_{UV}^{Uncorr}	SFR_{UV}^{Corr}
(1)	(2)	(3)	(4)	(5)	(6)	(7)	(8)
$0.9 < z \leq 1.2$	0.86 ± 0.2	-0.86	13.4	2.72	10.9 ± 2.5	1.2 ± 0.3	15.2 ± 3.5
$1.2 < z \leq 1.5$	1.93 ± 0.5	-0.50	27.0	3.44	44.8 ± 12	2.7 ± 0.7	62.7 ± 16.9
$1.5 < z \leq 2.0$	4.21 ± 1.4	-0.35	35.9	3.73	130 ± 44	5.9 ± 2.0	183.2 ± 60.9
$2.0 < z \leq 3.2$	8.00 ± 3.4	-0.78	15.7	2.88	113 ± 48	11.2 ± 4.8	158.3 ± 67.6

Note. — Column (1) indicates sample redshift range. Column (2) indicates uncorrected UV luminosity in units of 10^{28} erg s $^{-1}$ Hz $^{-1}$. Column (3) indicates the best fit slope, β , to the f_λ spectrum where $f_\lambda \propto \lambda^\beta$. Column (4) indicates the IR-UV ratio, S_{IR}/S_{1600} . Column (5) indicates the attenuation in magnitudes at 1600 Å derived from the best fit spectral index, β . Column (6) indicates the dust corrected UV luminosity in units of 10^{28} erg s $^{-1}$ Hz $^{-1}$. Column (7) and (8) refer to star formation rates derived from the UV luminosities in Columns (2) and (6) respectively, in units of M_\odot yr $^{-1}$.

Table 6. Redshift Binned sBzK Radio Luminosity and SFR Estimates

Redshift	$S_{1.4 \text{ GHz}}$	$S_{610 \text{ MHz}}$	α	$L_{1.4} \times 10^{22}$	$\text{SFR}_{1.4 \text{ GHz}}^{\text{Condon}}$	$\text{SFR}_{1.4 \text{ GHz}}^{\text{Bell}}$
Range	μJy	μJy	$S_\nu \propto \nu^\alpha$	W Hz^{-1}	$\text{M}_\odot \text{ yr}^{-1}$	$\text{M}_\odot \text{ yr}^{-1}$
(1)	(2)	(3)	(4)	(5)	(6)	(7)
$0.9 < z \leq 1.2$	$<2.26 \text{ (} 3\sigma \text{)}$	$<9.55 \text{ (} 3\sigma \text{)}$	-1.70 ± 1.67	<2.45	<38	<14
$1.2 < z \leq 1.5$	14.4 ± 1.8	25.2 ± 6.5	-0.66 ± 0.34	12.1 ± 1.7	139 ± 32	67 ± 9
$1.5 < z \leq 2.0$	10.0 ± 1.6	31.9 ± 9.8	-1.37 ± 0.41	29.6 ± 5.0	420 ± 248	164 ± 28
$2.0 < z \leq 3.3$	9.7 ± 2.3	19.7 ± 6.3	-0.84 ± 0.47	29.6 ± 7.1	359 ± 187	163 ± 39

Note. — Column (1) indicates the sample bin redshift range. Columns (2) and (3) indicate the median stacked flux at 1.4 GHz and 610 MHz respectively. 3σ upper limits are shown in the lowest redshift bin. Column (4) indicates the spectral index computed from these data. Column (5) indicates the derived rest frame 1.4 GHz luminosity. Column (6) indicates the computed $\text{SFR}(0.1\text{-}100 \text{ M}_\odot)$ according to Condon (1992). Column (7) indicates the computed $\text{SFR}(0.1\text{-}100 \text{ M}_\odot)$ according to Bell (2003). Upper limits are found for the $0.9 < z \leq 1.2$ flux measurements; these values are propagated to an upper limit SFR.

Table 7. Redshift Binned sBzK Star Formation Rate Summary

Redshift	SFR _{IR}	SFR _{24μm}	SFR _{UV}	SFR _{UV} ^{Corr}	SFR _{1.4GHz} ^{Condon}	SFR _{1.4GHz} ^{Bell}	SFR _{2–10keV} ^{Ranalli}	SFR _{2–10keV} ^{Persic}	SFR _{IR+UV}
(1)	(2)	(3)	(4)	(5)	(6)	(7)	(8)	(9)	(10)
$0.9 < z \leq 1.2$	11 \pm 2.8	9.9 \pm 2.6	1.0 \pm 0.3	15 \pm 3.5	<38	<14	9 \pm 8	45 \pm 40	12 \pm 2.8
$1.2 < z \leq 1.5$	55 \pm 7.0	89 \pm 8.5	3.0 \pm 0.7	63 \pm 17	140 \pm 32	67 \pm 9	12 \pm 6	60 \pm 30	58 \pm 7.0
$1.5 < z \leq 2.0$	95 \pm 14	190 \pm 51	6.0 \pm 2.0	180 \pm 61	420 \pm 250	164 \pm 28	32 \pm 11	160 \pm 55	100 \pm 14
$2.0 < z \leq 3.2$	120 \pm 28	760 \pm 85	11 \pm 4.8	160 \pm 68	360 \pm 190	163 \pm 39	107 \pm 23	535 \pm 115	130 \pm 28

Note. — Star formation rates for redshift binned sBzKs. Column (2) – SFR from integrated IR luminosity using CE01 template fits to MIR-radio photometry ($\lambda \geq 24\mu\text{m}$). Column (3) – SFR from CE01 template fit to 24 μm data only. Column (4) – SFR from UV continuum with no correction for dust. Columns (5) SFR from UV continuum with dust correction. Column (6) and (7) – SFR from median, stacked 1.4 GHz flux using the method of Condon (1992) and Bell (2003) respectively (1st row – a 3σ upper limit). Column (8) and (9) – SFR from hard band X-ray data using the method of Ranalli et al. (2003) and Persic et al. (2004) respectively. Column (10) – the total SFR from the sum of Column (2) and Column (4). Units are $\text{M}_{\odot} \text{ yr}^{-1}$ for all columns.